Advanced Steel Construction – Vol. 21 No. 5 (2025) 458–475
DOI:10.18057/IJASC.2025.21.5.8

EXPERIMENTAL AND NUMERICAL STUDY ON CONNECTION JOINTS APPLIED TO AUTOMATIC CONSTRUCTION DEVICE

Xian-Feng Wang [1], Qian-Xi Zhang [1], Zhi-Peng Fu [1], Wei-Lun Wang [1, *], Jian Liu [1], Xiao-Gang Zhang [1] and Shan-Bai Dong [2]

[1] Guangdong Provincial Key Laboratory of Durability for Marine Civil Engineering, State Key Laboratory of Intelligent Construction and Healthy Operation and Maintenance of Deep Underground Engineering, College of Civil and Transportation Engineering, Shenzhen University, Shenzhen 518060, China

[2] Excellence Group Co. Ltd. Shenzhen 518052, China

** (Corresponding author: E-mail address: wang_weilun@hotmail.com)*

ABSTRACT

To meet the demands of intelligent and green construction, the development of automatic construction devices is of practical significance. In this study, a novel connection joint was designed for its supporting column and investigated experimentally and numerically based on static load tests, which were carried out on five joint specimens with different axial pressure ratios, flange thicknesses, and insertion depths. It was found that the failure of all specimens was due to the bolted connection, especially the failure of the thread. However, no apparent damage was found on the tube wall of the joint, indicating that the damage mainly occurred at the bolt connection. Additionally, a finite element analysis (FEA) model was established to investigate the joint's failure process, revealing intricate stress and strain conditions under loading. Notably, the highest stress and strain were identified at the central bolt, indicating its critical role in joint failure. The parameters of tube wall thickness and flange outside diameter in the finite element model were analyzed, and the results showed that 10 mm wall thickness and 252 mm outer diameter of flange were the best choices. This study may provide an experimental and numerical basis for the practical application of automatic construction devices.

ARTICLE HISTORY

Received:	21 September 2024
Revised:	22 February 2025
Accepted:	22 February 2025

KEYWORDS

Automatic construction device;
Steel joint;
Static load tests;
Finite element analysis;
Moment-rotation relationship

1. Introduction

Currently, the civil construction industry is facing various challenges, including substandard construction site conditions, high hazards, environmental pollution, and elevated construction costs [1-4]. Increasing automation in the construction process is a vital strategy to address these issues. The development of automation and intelligent technologies has significantly changed the construction industry [5-9]. Various construction robots, such as wheeled robots, wall-building robots, and welding robots, have been invented by researchers. Advanced automation devices have played a critical role in protecting workers from hazardous and physically demanding tasks [10] while markedly increasing productivity [11]. However, these robots are generally limited to specific tasks within the construction process. To further enhance automation across the entire construction process, improve working conditions, and reduce costs, highly integrated automated construction devices have been progressively applied by various countries since the late 20th century [12-17]. These devices aim to increase the overall automation level of the construction process.

In the last century, an automated construction device known as Big Canopy was developed in Japan [13], which was used in the construction of concrete buildings. This device utilized precast concrete (PC) components installed using remote control, significantly reducing the required labor force. Bar codes marked on the components enabled precise monitoring of their positions during construction, significantly improving construction efficiency. In recent years, several automated construction devices have been independently developed in China [17, 18]. These devices predominantly use cast-in-situ reinforced concrete to ensure structural stability and safety. Material transport, formwork operations, and concrete pouring are all controlled by computer programs. This high level of automation has significantly enhanced construction efficiency and reduced costs. However, deficiencies remain in the design of the connection joints of the support columns in current automated construction devices. These joints do not adequately support the continuous lifting of support columns as building height increases. Additionally, the connection process of the support columns presents many inconveniences, resulting in low installation efficiency. Given the existing issues of the support column device in the current automatic construction device, a new type of joint has been designed in this paper, which aims to enhance the automation level of the automatic construction device.

There have been numerous researches on beam-column connection joints, which share similarities with the support column connection joints in automatic construction devices in terms of structural form and mechanical characteristics. For steel beam-column joints, researchers have studied different configurations of reinforced panels and flange panels to identify joints with enhanced energy consumption [19-23]. Some researchers have introduced replaceable energy dissipation devices at beam-column joints to enable repairability in case of joint damage. Test results have shown that these devices exhibit good energy dissipation capacity and repairability [24]. Another connection method involves the use of sleeves and bolts for convenient installation. Zhang et al. [25] proposed a design method for core tube flange column joints, where the separation of connecting flange plates was further controlled by incorporating prestressed tendons into the column joints, yielding positive outcomes in joint performance. Fan et al. [26] presented a square steel tubular column-column joint with a blind bolt connection. The upper and lower columns were connected to the joint using four connecting plates and bolts, verifying good sliding resistance and ultimate bearing capacity.

The demonstration project of an automatic construction device currently utilizes a joint connection form depicted in Fig. 1. However, the connection exhibits relatively low connection strength as it only relies on the three bolts within the connection. Additionally, the necessity for attaching the connecting bracket to the building entails drilling into the concrete. These requirements render field installation both inconvenient and time-consuming.

This study proposed a novel connection joint designed explicitly for the automatic construction device, aiming to elevate its automation level, as illustrated in Fig. 2. The primary objective of this design is to enhance the installation convenience of the lifting column standard section while accommodating the lifting requirements of the support column. During installation, the bolt holes automatically align when the four corners of the upper and lower lifting column standard sections are properly aligned and inserted. The two lifting column standard sections are then connected by bolts. This joint design not only facilitates easier installation but also meets the demands of the support column lifting installation inherent to the automatic construction device. Furthermore, a pulley has been integrated at the end of the horizontal support frame of the automatic construction device, as illustrated in Fig. 3. This pulley interfaces with the track affixed to the building, enabling the entire support structure to be lifted upward as each lattice column standard section is installed from below. This feature facilitates the construction of higher floors, enhancing the overall efficiency and versatility of the device and also meeting the needs of a high automation level of the automated construction device.

In this paper, the mechanical behaviors of the newly designed connection joint, focusing on five steel joint specimens with distinct geometric parameters, were systematically analyzed and compared. Both static load tests and finite element analysis were employed to examine the mechanical properties and failure modes of the specimens. The experimental data were subsequently corroborated and expanded upon using finite element analysis to provide a more comprehensive understanding of the performance of the joint under diverse conditions, such as varying tube wall thickness and flange outside diameter. The impact of these additional parameters on the mechanical properties of the joints was estimated using the finite element method. By understanding the performance of these joints under various conditions and parameters, it became feasible to optimize their design and enhance the safety and reliability of the automatic construction device during construction operations.

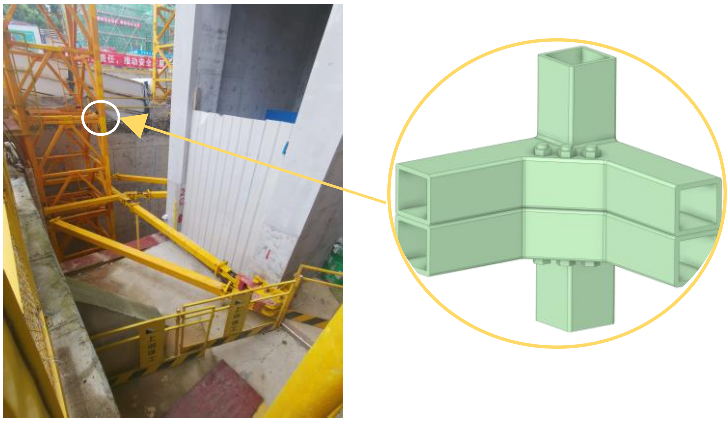

Fig. 1 Connecting joint of automatic construction device project

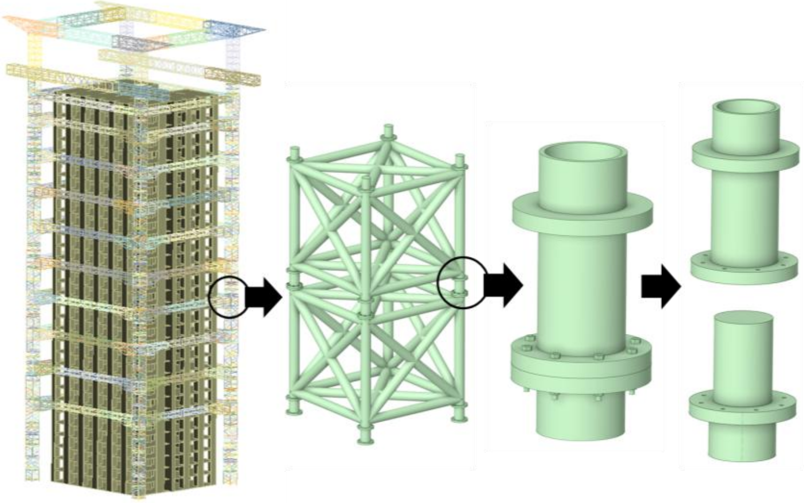

Fig. 2 A new type of connection joint for the automatic construction device

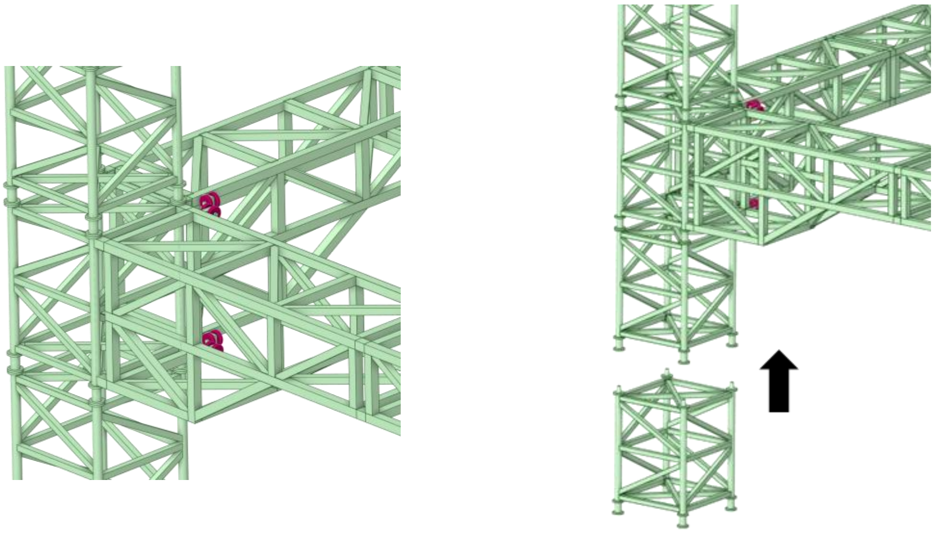

Fig. 3 Schematic diagram of the lifting process of the automated construction device

2. Experimental study

2.1. Test specimens

A novel connection joint was designed to enhance the automation level of the automated construction device, as illustrated in Fig. 4. The connection joint was assembled from two parts. The upper part, a seamless steel tube, was welded to the flange-A at its bottom, while the lower part, also a seamless steel tube, was welded to the inserting portion with the flange-B at the welding site. Notably, during assembly, the inserting portion, a top-closed seamless steel tube, was inserted into the cavity of the upper seamless steel tube at the joint. The upper and lower parts of the joint were then connected by eight high-strength bolts.

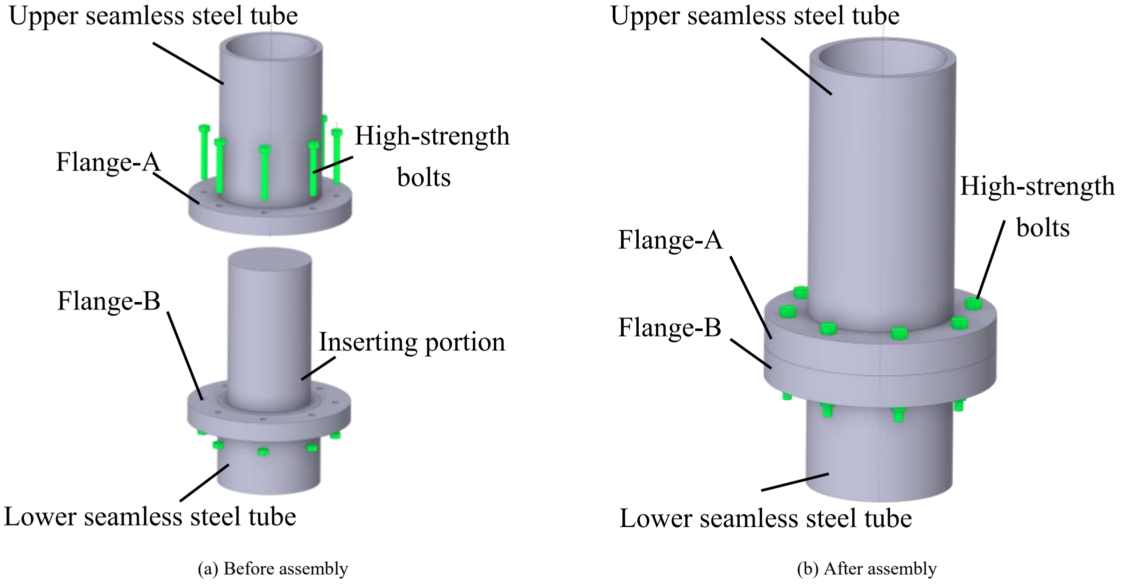

(a) Before assembly (b) After assembly

Fig. 4 Configuration of connection joint

Whether dealing with seamless steel tubes or flange plates, the curved outer surface posed a challenge when connecting to the horizontal actuator of the testing machine. To address this, a circular ring was welded on the outer surface of the seamless steel tube at the upper part of the joint. Subsequently, a horizontal connector was designed, as illustrated in Fig. 5. This connector, consisting of two bolt-connected parts, formed a circular cavity that snugly encased the welded ring on the upper part of the joint, thus facilitating the connection between the horizontal actuator and the joint. Additionally, an end plate with pre-designed bolt holes was welded to the top of the joint, enabling connection to the vertical actuator. During loading, the material experienced increasing bending moments further from the horizontal loading position, leading to substantial bending moments at the bottom of the joint. A single-end plate welded at the bottom of the joint proved insufficient, often resulting in weld failure before the joint was fully stressed [27]. To overcome this, two flanges (Flange-C and Flange-B) were welded at the bottom of the joint, and eight stiffeners were interposed between them. These plates allowed eight bolts to pass through, effectively securing the bottom of the joint.

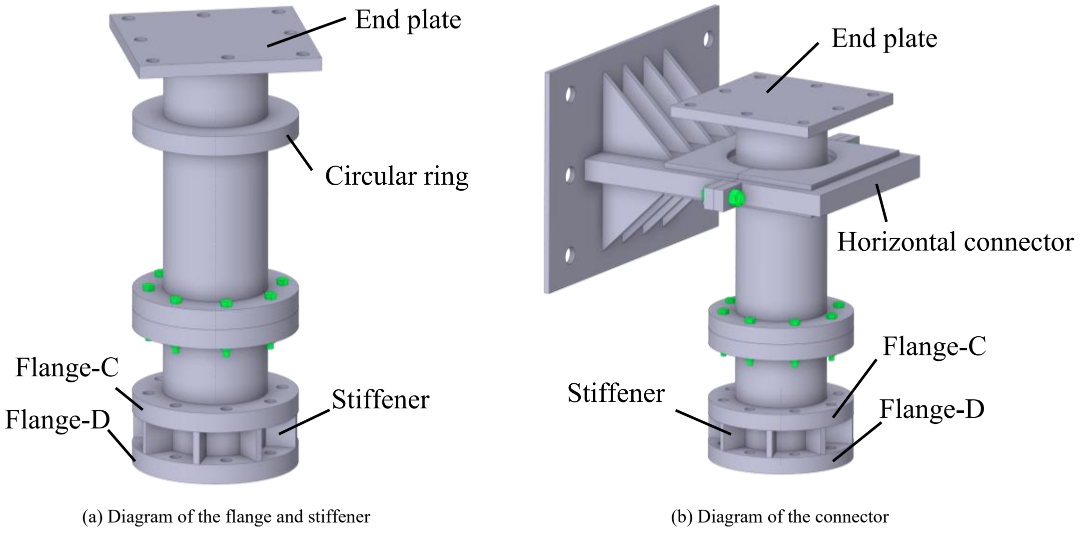

(a) Diagram of the flange and stiffener (b) Diagram of the connector

Fig. 5 Joint connected to the testing device

In this study, five steel joint specimens were tested. These specimens were designed to have the same height and outside diameter as the seamless steel tube. The length of the upper seamless steel tube of all specimens is 420 mm, and the length of the lower seamless steel tube of all specimens is 470 mm. All specimens are constructed from 20# seamless steel tubes specified in GB/T 8162-2018 [28], and all the flanges and stiffeners of all specimens are made of Q345B steel specified in GB/T 1591-2018 [29]. For specific material properties, see Tables 1 and 2.

The five specimens differed in the parameters of the flange-A and flange-B thickness, the axial compression ratio, and the inserting portion depths. Notably, the change in axial compression ratio was achieved by varying the vertical axial force magnitude. These parameters significantly influenced the mechanical properties of the joints [30-34]. The specific size parameters of all specimens are shown in Fig. 6 and Table 3, where t is the wall thickness of the seamless steel tube, h is the thickness of flange-A and flange-B, and F is the magnitude of the vertical axial force acting on the top of the joint specimen.

The axial pressure was estimated based on the specific application scenario. By considering the combined dead weight of the entire framework, along with the additional loads from the upper equipment, materials, and personnel, the vertical force exerted at the bearing column joint has been calculated to be 600 kN. To analyze the structural performance under varying loads, two additional vertical axial force values of 400 kN and 800 kN were selected. Regarding the flange thickness, given that a range of 15-30 mm was typically utilized for steel structure end plates and similar components, thicknesses of 20 mm and 30 mm were chosen for further investigation [35-42].

Eight high-strength bolts between flange-A and flange-B are 10.9 s M10 ones [26]. A torque wrench was used to apply torque to the bolt. The designed pretension was 55 kN, and the actual pretension ranged from 46.7 kN to 63.6 kN, calculated by the actual torque applying the bolt preload, according to GB/T 1231-2006 [43].

Table 1
Material properties of the steel plate

	Chemical component (%)							Yield strength (MPa)	Ultimate strength (MPa)	Elongation (%)
Steel Q345	C	Si	Mn	P	S	Cu	Nb	407	555	26.5
	0.1600	0.2100	1.3900	0.0150	0.0020	0.0400	0.0030			
	V	Ti	Cr	Mo	Ni	Als	CEV			
	0.0010	0.0230	0.0400	0	0.0017	0.0005	0.4000			

Table 2
Material properties of the seamless steel tube

Specification (Outer diameter * thickness.) (mm)	Chemical component (%)								Yield strength (MPa)	Ultimate strength (MPa)	Elongation (%)
	C	Si	Mn	P	S	Ni	Cr	Cu			
133*10	0.210	0.190	0.480	0.028	0.009	0.009	0.023	0.011	300	497	23
159*10	0.200	0.200	0.560	0.011	0.008	0.020	0.060	0.020	374	632	18

Table 3
Detailed information of the specimens (Fig. 6)

Specimen No.	t (mm)	h (mm)	s (mm)	F (kN)
J-1	10	30	200	400
J-2	10	30	200	600
J-3	10	30	200	800
J-4	10	20	200	400
J-5	10	30	100	400

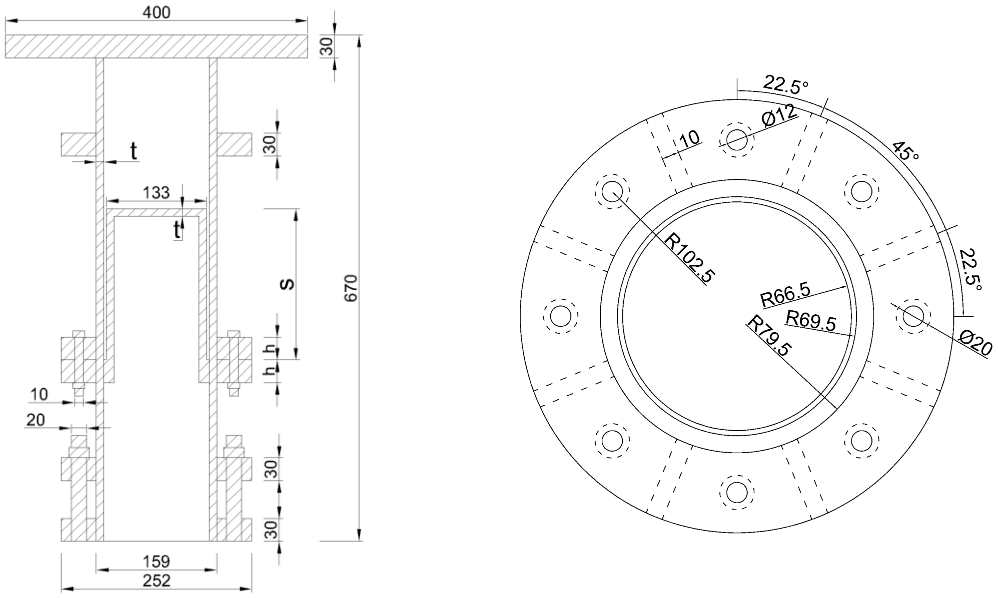

(a) Section view of the specimen (mm)

(b) Top view of the specimen (mm)

Fig. 6 Structural diagram of a connection joint

2.2. Test setup and loading scheme

The experiment was performed in the Structural Laboratory of the College of Civil and Transportation Engineering at Shenzhen University, as shown in Fig. 7.

The vertical actuator with a load capacity of 2000 kN was connected to the top-end plate of specimens by eight high-strength bolts and exerted a constant vertical force on the top of the specimens. Similarly, a horizontal actuator, capable of exerting up to 1500 kN, was connected to the specimens by a horizontal connector and applied a horizontal force or displacement.

Before the horizontal static loading test, an axial force was constantly applied to the specimen by a vertical actuator throughout the entire test loading process. The specimen was preloaded by the horizontal actuator, which first applied horizontal thrust from 0 to 20 kN through the force control mode and then unloaded to 0. The slippages between the steel plate at the lower fixed end and each bolt were eliminated by the preloading process. A horizontal displacement was then applied to the specimen by the horizontal actuator through the displacement control mode, and a loading rate of 1 mm/min. The loading process was terminated until the force applied was reduced to 85% of the ultimate bearing capacity of the specimen.

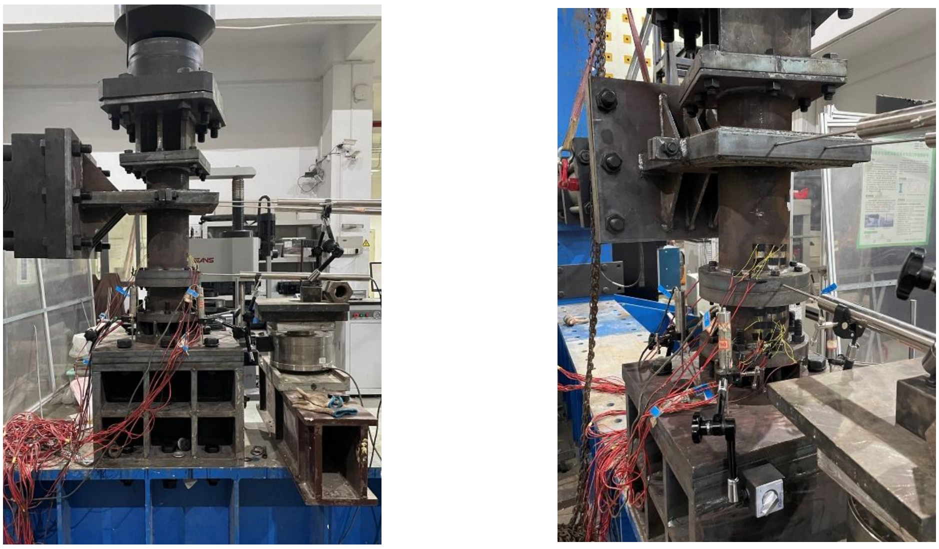

(a) Front view (b) Lateral view

Fig. 7 Test setup for a connection joint

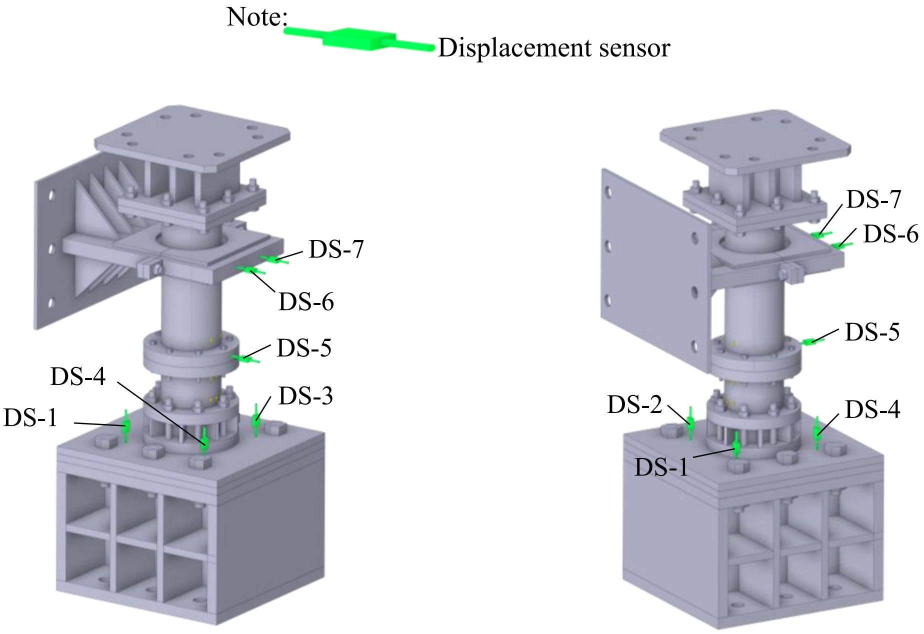

(a) Front view (b) Lateral view

Fig. 8 Displacement sensor layout of the specimen

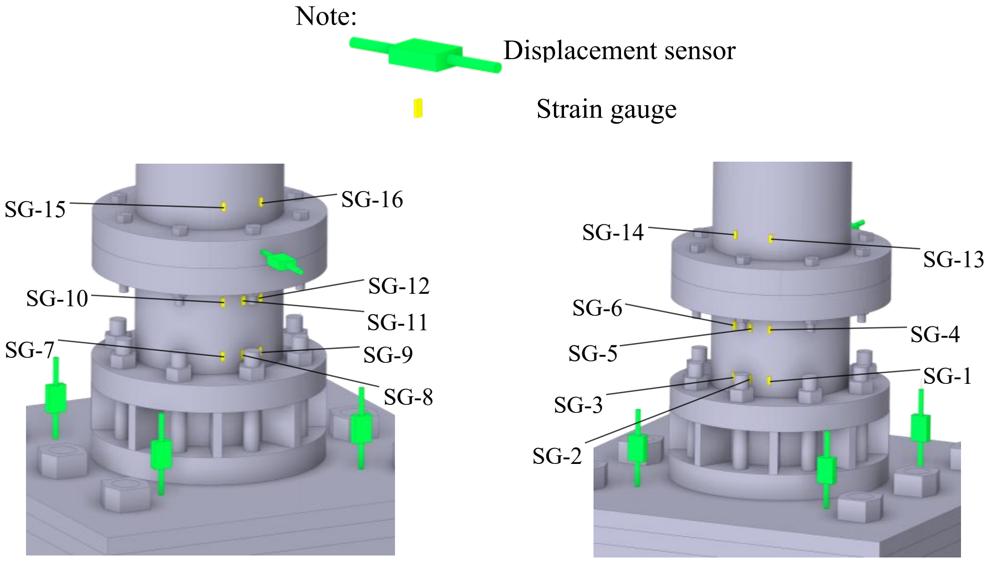

(a) Front view (b) Lateral view

Fig. 9 Strain gauge layout of the specimen

2.3. Measurement scheme

The measurement scheme of the five specimens is identical, and the layout of displacement sensors is shown in Fig. 8. The vertical height of the two displacement sensors (DS-6 and DS-7) was the same, and they were placed at the front and back sides to measure the horizontal displacement at the loading position, with the average value used as the horizontal displacement. Four displacement sensors were placed around the lower fixed part of the specimen to measure the buckling that might occur in the bottom plane of the specimen.

Each specimen in the study was outfitted with 16 strain gauges. These gauges were strategically distributed on the outer surface of the circular tube of the specimens. The precise locations of the strain gauges are depicted in Fig. 9.

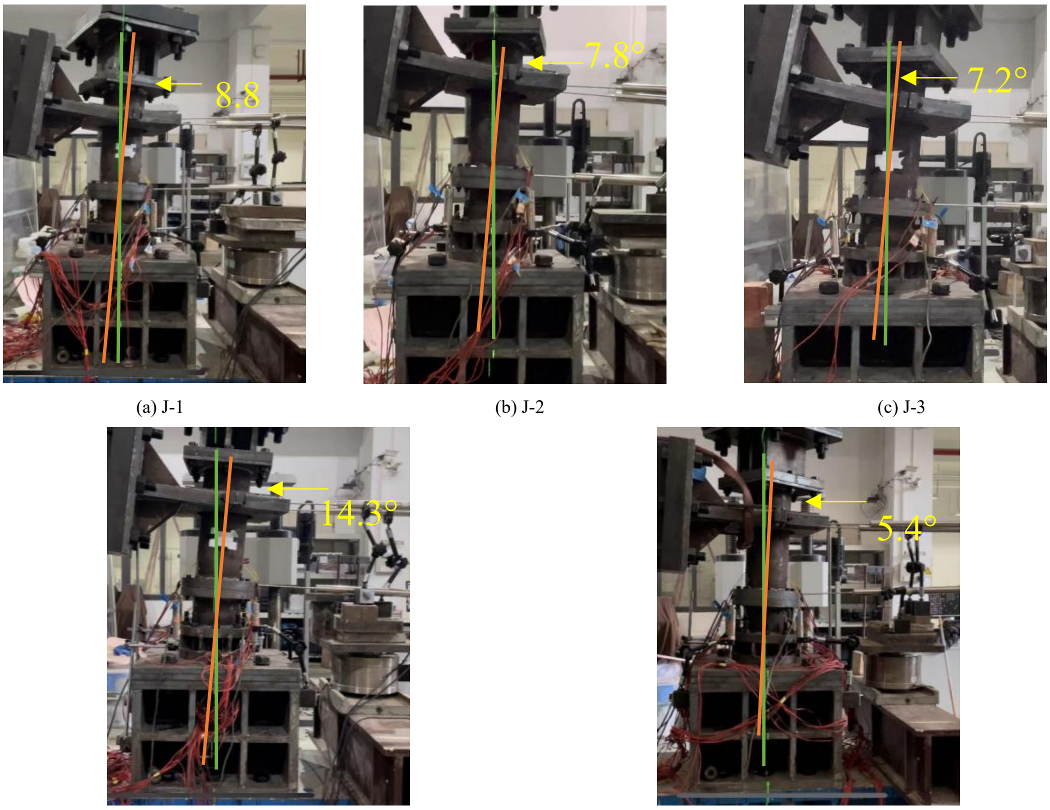

(a) J-1 (b) J-2 (c) J-3

(d) J-4 (e) J-5

Fig. 10 Rotation angle of the joints after loading. (In the figures, the green line represents the specimen's initial axial position, determined based on the light emitted from a gradienter before the experiment. The orange line indicates the vertical line of the middle flange plate of the joint specimen after the experiment.)

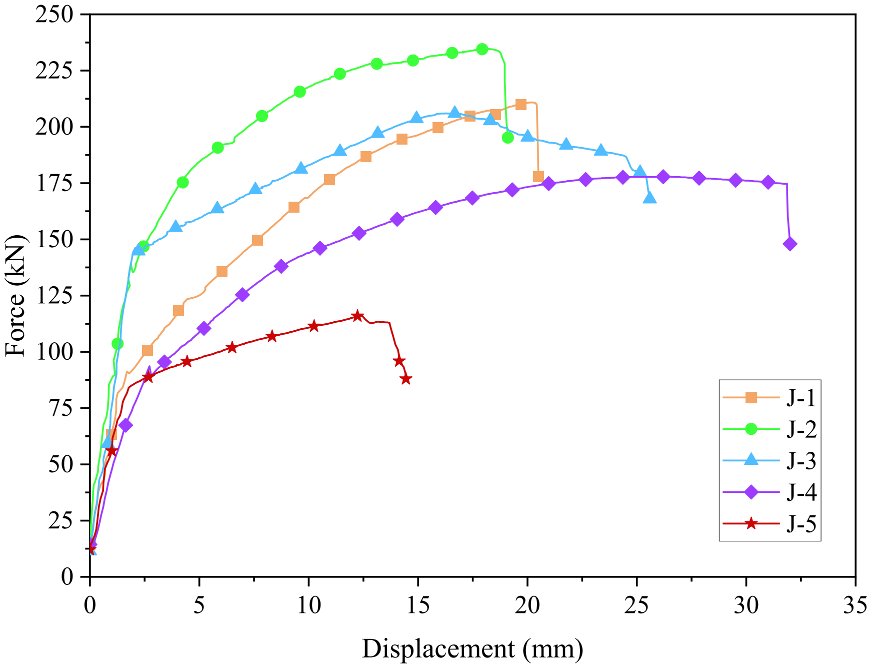

Fig. 11 Load-displacement curves of the specimens

3. Experimental results

3.1. Observed joint performance and discussion

During the experiment, different specimens exhibited varying rotation angles upon the application of the horizontal actuator, as illustrated in Fig. 10. The angular difference between the green and yellow lines signifies the extent of the specimen's rotation.

Notably, as the axial pressure ratio increased, the rotation angle of the joint decreased sequentially from 8.8° to 7.8°, and ultimately to 7.2°, with corresponding reduction rates of 11.4% and 18.2%, respectively, indicating a diminishing rotational capacity of the joint. Conversely, reducing the flange thickness of the joint by 10 mm significantly increased the rotation angle to 14.3°, a rise of 62.5%, thereby enhancing the rotational ability of the joint. Furthermore, halving the length of the inserting portion of the joint reduced the rotation angle to 5.4°, a decrease of 38.6%, thus weakening the rotational capability of the joint. Observation of the test indicated that none of the specimens exhibited apparent signs of damage after testing. However, during the disassembly process, it was discovered that the bolts between flange-A and flange-B in the middle of the joints had loosened.

3.2. Load versus displacement curves

The average value of the results of the two parallel displacement sensors (DS-6 and DS-7) on both sides of the upper part of the specimen was taken as the horizontal displacement of the specimen, and the load-displacement curve of the specimen was drawn, as shown in Fig. 11. As the ultimate bearing capacity of the specimen dropped to 85%, the test was stopped, so the load-displacement curve only had a small decreasing section. However, in the actual loading process of the specimen, the bearing capacity of the specimen showed a zigzag and repeated decreasing trend. The yield displacement, yield strength, ultimate displacement, and ultimate strength of each specimen were listed in Table 4. Among them, yield displacement and yield strength refer to the transverse and longitudinal coordinate values at the apparent turning point of the load-displacement curve of the specimens.

From the load-displacement curves of each specimen, a linear segment characterized the initial loading stage, indicating the elastic behavior of the specimens. As loading progressed, the curves evolved into nonlinear segments, reflecting the onset of local plastic deformation in the joints. In load-displacement curves of the J-3 specimen exhibited a gradual decline compared to the other four specimens, which showed a sharp decrease after reaching their ultimate bearing capacity.

Table 4
Mechanical parameters of the specimens

No.	Yielding strength (kN)	Yielding displacement (mm)	Ultimate strength (kN)	Ultimate displacement (mm)
J-1	91.3	1.695	210.9	20.209
J-2	139.1	1.873	234.6	18.711
J-3	146.3	2.082	206.0	16.591
J-4	93.6	2.724	177.8	26.580
J-5	84.1	1.771	116.2	12.345

With the progressive increment of axial pressure ratio, a significant escalation in the yield strength of the joint was observed, rising from 91.3 kN to 139.1 kN, and ultimately reaching 146.3 kN, marking increases of 52.4% and 60.2%, respectively. Correspondingly, the yield displacement of the joint demonstrated a parallel upward trend, registering increases of 10.5% and 22.8%. These findings indicated a positive correlation between the axial pressure ratio and yield strength and displacement within a defined range, with a notably more substantial influence on the yield strength. Conversely, the relationship between axial pressure ratio and ultimate strength and ultimate displacement exhibited a distinct pattern. As the axial pressure ratio increased, the change rate in ultimate strength was relatively small, recorded at 11.2% and -2.3%, respectively. This modest variation could be further influenced by potential eccentricity effects at the initial stage, suggesting that axial force exerted a limited impact on the ultimate strength of joints. Moreover, an increase in axial force was associated with a continual decrease in ultimate displacement, indicating an earlier joint failure. This was attributed to the influence of second-order effects caused by the vertical load.

When the thickness of the joint flange was decreased by 10 mm, an increase of 2.5% in the yield strength and a significant increase of 60.7% in yield displacement were observed. The specimen exhibited a 15.7% decrease in ultimate strength and a 31.5% increase in ultimate displacement when it reached the limit state. These changes suggested that a reduction in flange thickness markedly enhanced the ductility of the joint. Conversely, when the insertion depth of the joint was halved, the yield strength of the specimen decreased by 7.9%, yield displacement increased by 4.5%, ultimate strength decreased by 44.9%, and ultimate displacement reduced by 38.9%. These results indicated a substantial reduction in both the strength and ductility of the joint due to the halving of insertion depth, an unfavorable outcome in practical applications.

3.3. Deformation curve of the bottom plate

Displacement measurements captured by sensors DS-1, DS-2, DS-3, and DS-4 on the bottom plate of various specimens are shown in Fig. 12. According to the positions of the four displacement sensors in Fig. 8, it can be found that under ideal conditions, the values of the sensor DS-1 and DS-2 on the tension side are the same and positive, while the values of the sensor DS-3 and DS-4 on the compression side are the same and negative. If the values of the four displacement sensors are not this law, it indicates that the bottom plate is bulging.

As shown in Fig. 12a and b, sensors DS-1 and DS-2, positioned on the tension side of the material, registered positive values due to the base plate being stretched upward. A reduction in the displacement on the tension side of the base plate was observed as the axial pressure ratio increased. This reduction was attributed to the downward force exerted by the axial pressure, which limited the tensile displacement of the base plate. This observation aligned with the phenomenon noted in the test, where an increase in the axial pressure ratio resulted in a reduction of the rotation angle of the joint. For joint J-4, the measurement values from DS-1 and DS-2 were significantly higher. This indicated that a decrease in the thickness of the flange correlated with an enhancement in the bulging of the bottom plate, consistent with the observed increase in the rotation angle during the test. Fig. 12c and d demonstrated that DS-3 and DS-4 were positioned on the compression side of the material, where the bottom plate experienced downward compression, yielding negative displacement values. For joint J-5, torsion of the specimen was observed, causing a significant discrepancy between the measurements of displacement sensors DS-1 and DS-2, and a positive displacement value for DS-3. As depicted in Fig. 12c and d, the displacement measurements for each specimen did not exhibit a clear pattern of regularity. This lack of uniformity was attributed to the base plate not being perfectly planar, with bumps or depressions on its surface. These irregularities resulted in non-uniform displacement when the bottom plate was compressed. This issue was not observed on the tension side of the base plate. This should be attributed to losing contact with the ground when the base plate was stretched. Consequently, any surface defect on the base plate did not influence its displacement under this condition.

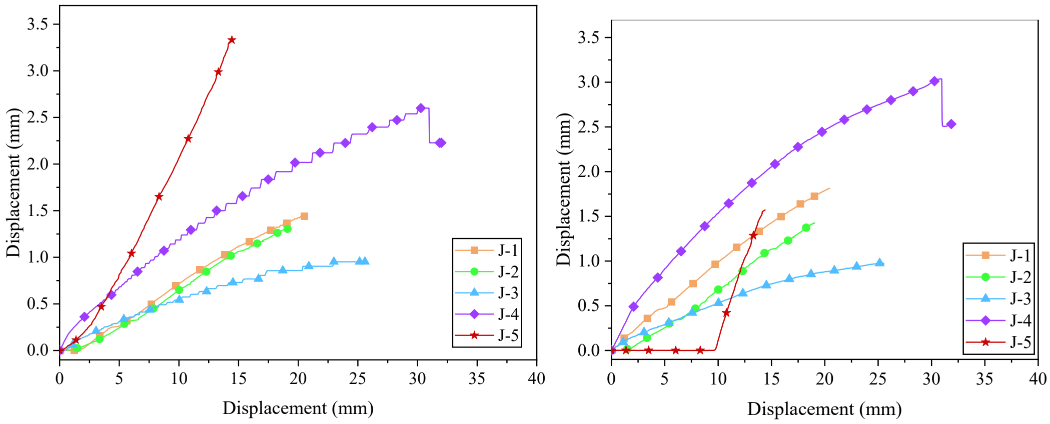

(a) Displacement value of DS-1 (b) Displacement value of DS-2

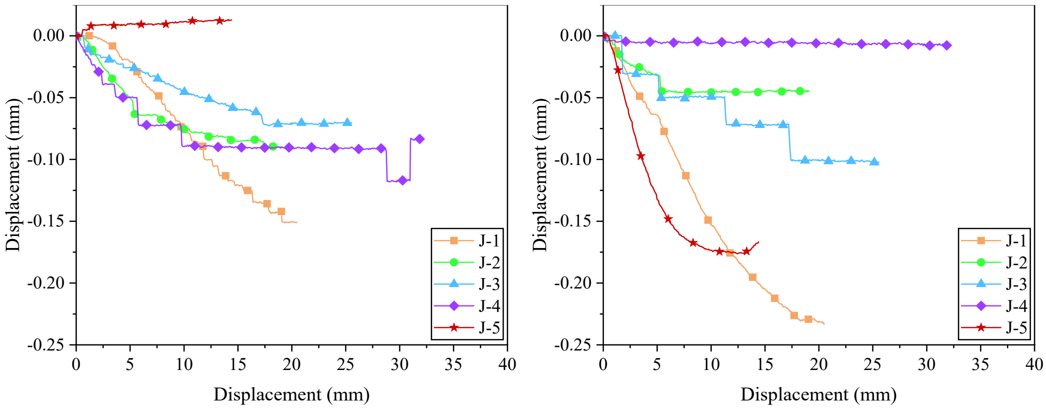

(c) Displacement value of DS-3 (d) Displacement value of DS-4

Fig. 12. Deformation displacement curve of the bottom plate. (In the figure, the horizontal coordinate is the average value of DS-6 and DS-7, and the vertical coordinate is the measured value of DS-1, DS-2, DS-3, and DS-4, respectively)

3.4. Moment versus rotation curves

In the analysis presented in the abovementioned section, it was observed that warping of the bottom plate resulted in an increased angle at the joint. To accurately determine the actual rotational capacity of the joint and construct the moment-angle curve, the rotation attributable to the buckling of the bottom plate was approximately eliminated using methods depicted in Eqs. (1) and Fig. 13. Notably, due to the progressive horizontal displacement at the top, the ground rotation center of the joint did not align with the central axis of the joint. Instead, it shifted towards the compression area.

$$\theta = \frac{L_a}{L_h} - \frac{L_t + L_p}{L_s} \tag{1}$$

where L_t is the mean value of DS-1 and DS-2 displacement sensor; L_p is the mean value of DS-3 displacement sensor and DS-4 displacement sensor; L_a is the mean value of DS-6 displacement sensor and DS-7 displacement sensor; L_h is the distance from the middle of the ring to the top of flange-C; L_s is the distance between DS-1 and DS-4 (the distance between DS-2 and DS-3) that is 250 mm. θ is the actual rotation of the joint.

The moment-rotation curves of the joints are shown in Fig. 14, and the mechanical properties of each specimen are given in Table 5, where K_0 represents the initial rotational stiffness of the joint (the slope of the line segment in the moment-rotation curve), K_1 represents the tangent stiffness of the joint (the tangent slope of the load-displacement curve at the initial stage of bending), M_y represents the yield moment, θ_y represents the yield rotation, M_u represents the ultimate moment, θ_u represents the ultimate rotation.

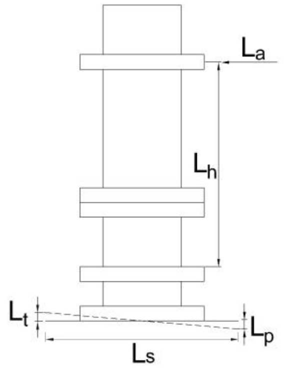

Fig. 13 Definition of L_t, L_p, L_a, L_h, L_s

Table 5
Mechanical parameters of the specimens

Specimen No.	K_0 (kN·m/rad)	K_1 (kN·m/rad)	$\frac{K_1}{K_0}$	M_y(kN·m)	θ_y(rad)	M_u(kN·m)	θ_u(rad)
J-1	11615	2783	0.240	47.93	0.0037	110.72	0.0457
J-2	15944	4273	0.268	73.03	0.0038	123.17	0.0403
J-3	15973	1196	0.075	76.81	0.0047	108.15	0.0350
J-4	6037	1826	0.302	49.14	0.0073	93.35	0.0613
J-5	10509	732	0.070	44.15	0.0037	61.01	0.0313

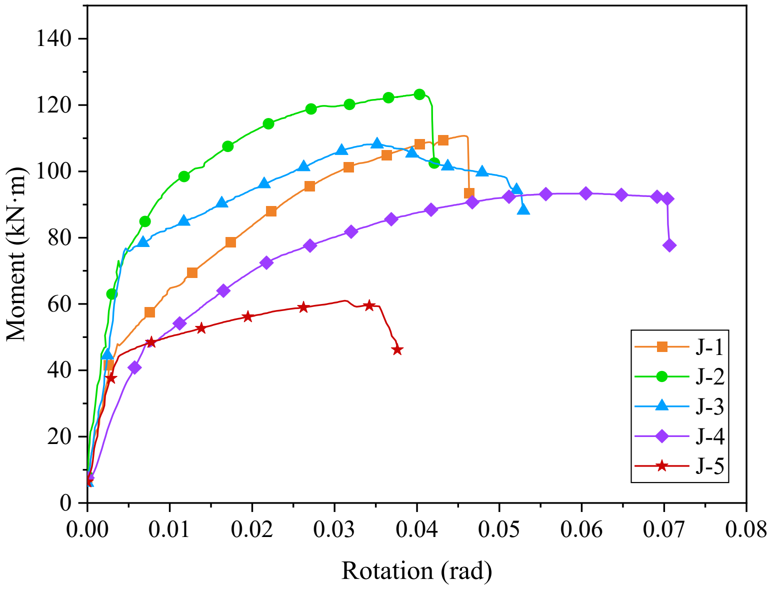

Fig. 14 Moment-rotation curves of the joints

As axial pressure increased, the initial stiffness, yield moment, and yield displacement of the joint rose, indicating enhanced elastic strength and deformation capacity. Compared with specimen J-1, the ultimate bending moment of the joint increased by 11.2% and subsequently decreased by 2.3%, suggesting that the effect of axial pressure on the ultimate bending moment initially escalated and then diminished under a specific axial force. A reduction of 11.8% and 23.4% in the limit angle was observed, implying that higher axial pressure precipitated the earlier failure of the joint. A notable decrease in the stiffness of the specimen was observed once it entered the plastic state. As evidenced in Table 5, an increase in axial force to 800 kN markedly reduced the stiffness of the joint, with its tangential stiffness being just 0.075 times its initial stiffness. Despite no significant variation in the load-bearing capacity of the joint, this abrupt decline in stiffness invariably accelerated joint failure. A decrease in the flange thickness of the joint resulted in higher yield bending moments and angles, while the initial stiffness dropped by 48.0%, nearly halving. The ultimate load-bearing capacity decreased by 15.7%, while its ultimate angle rose by 34.1%. This indicated a trade-off in the joint, sacrificing ultimate strength for greater rotational capacity. The ratio of tangential to initial stiffness of the joint rose to 0.302, indicating a lesser decrease in the stiffness of the joint. Halving the insertion depth of the joint led to reduced load bearing and rotational capacities, making it inadvisable in practical applications.

4. Finite element analyses

4.1. Finite element model

The finite element models simulating the loading of joints were built as shown in Fig. 15. The hexahedral element of twenty nodes was used to mesh circular steel tubes, flanges, stiffeners, and bolts. The global mesh size was 10 mm, and the refinement size was 5 mm and 2 mm for the bolts and bolt holes. In this study, the high-strength bolts were simplified into a dumbbell-shaped solid model, and the bolt modeling excluded the gaskets. The stress-strain model of steel and high-strength bolts is shown in Fig. 16. The elastic modulus of steel and high-strength bolts was 206 GPa, and Poisson's ratio was 0.3. The pretension force within all the high-strength bolts in the finite element model adopted a design value of 55 kN. In the finite element model, the bolt pretension force was applied to the surface of the bolt rods. The boundary condition of the lower part of the finite element model was simplified to consolidation, constraining the displacement in all directions, in which the degrees of freedom in the vertical direction of the upper part of the specimen and the rotation direction of the bending plane were released.

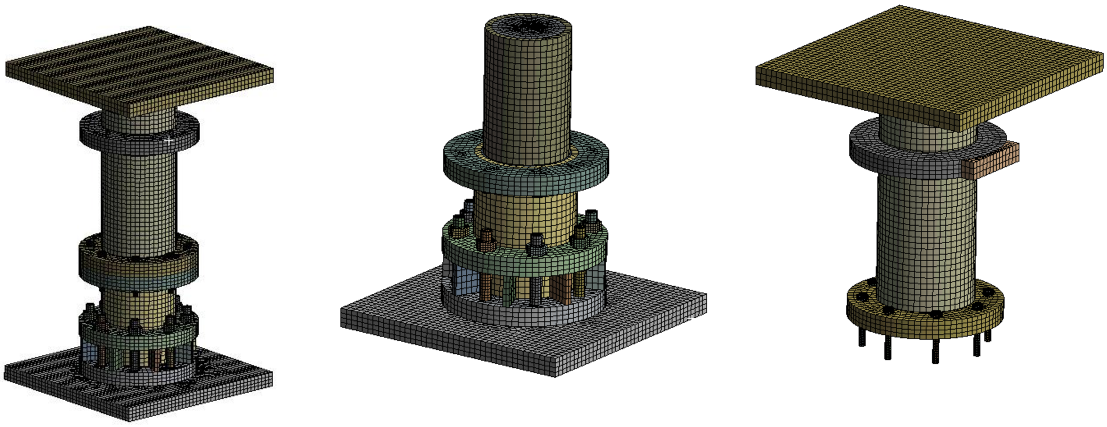

(a) Overall joint model (b) Lower part (c) Upper part

Fig. 15 Finite element models for the proposed joint

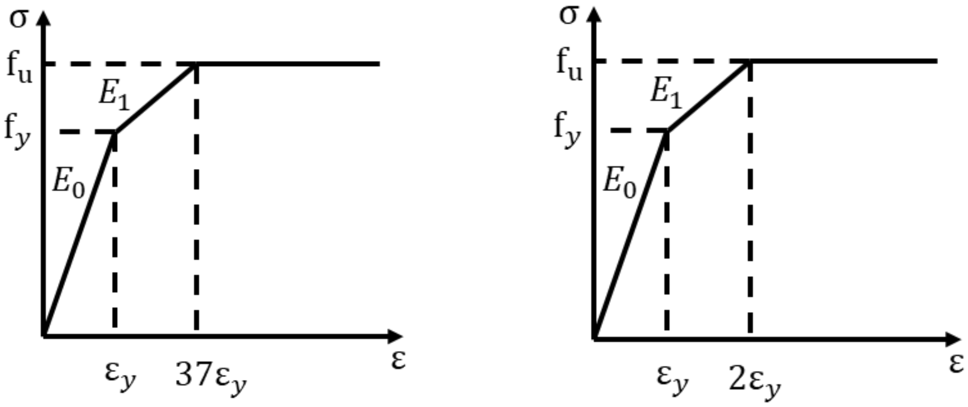

(a) Stress-strain curve of steel (b) Stress-strain curves of high-strength bolts

Fig. 16 Constitutive model of the materials

4.2. Finite element model validation

The mechanical behavior of all five specimens was simulated using the finite element method (FEM). Fig. 17 compared the load-displacement curves between the test and finite element results for the specimens. The mechanical parameters obtained by simulation and the comparison between test parameters and simulation parameters are shown in Table 6. As can be seen from Fig. 17 and Table 6, the simulation results were in good agreement with the test results, though there were still some gaps, which might have resulted from the initial defects in the test specimens and the gaps between the combined structures. Additionally, in the process of numerical simulation modeling, the simplification of the bolt model in the simulation and the selection of the norm value of the friction coefficient also contributed to the difference between the experimental and simulation results.

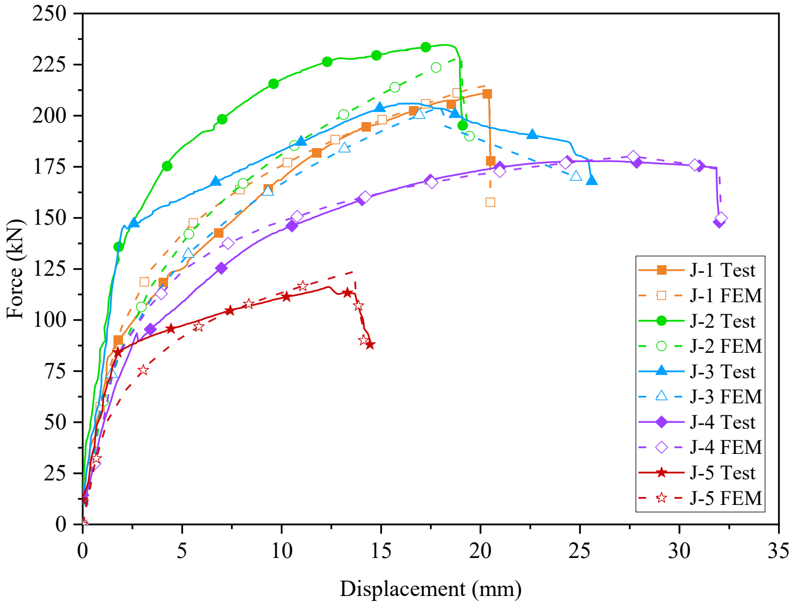

Fig. 17 Comparison of load-displacement curves between test and simulation

Table 6

Comparison between test result parameters and simulation result parameters

Specimen No.		J-1	J-2	J-3	J-4	J-5
K_0 (kN/mm)	Test results	57.08	58.98	61.77	46.92	51.92
	Simulation results	56.85	58.99	62.95	46.34	48.69
	Deviation (%)	-0.40	0.02	1.91	-1.24	-6.22
Peak strength (kN)	Test results	210.91	234.61	206.00	177.81	116.20
	Simulation results	215.00	229.00	204.33	180.01	123.57
	Deviation (%)	1.94	-2.39	-0.81	1.24	6.34
Peak displacement (mm)	Test results	20.21	18.71	16.59	26.58	12.34
	Simulation results	20.45	19.04	17.96	27.52	13.60
	Deviation (%)	1.19	1.76	8.25	3.54	10.17

4.3. Finite element results analysis

The stress-strain distribution characteristics of each test specimen were obtained via the aforementioned finite element simulation. For the joint specimen, the middle bolt and the compression side of the lower steel pipe were identified as potential locations for higher stress and strain occurrence. Therefore, the stress-strain distribution of these two places was analyzed and was detailed below. The schematic diagram of the middle bolt and the lower steel pipe compression zone is shown in Fig. 18.

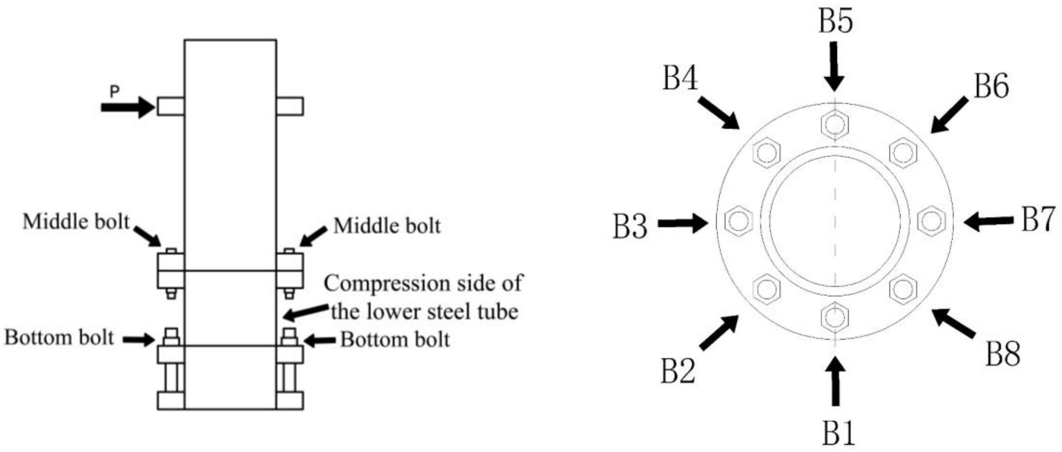

(a) Diagram of bolt position

(b) Numbering diagram of the middle bolts

Fig. 18 Position diagram of bolts and steel pipe pressure zone

As shown in Fig. 18, owing to the application of a horizontal force on one side of the specimen, the material of the specimen was stretched on the side facing the horizontal force and compression on the opposite side. Fig. 18(b) presents the top view of Fig. 18(a). B1 to B8 represent eight middle bolts. Bolts B2 to B4 experience tensile stress, whereas bolts B6 to B8 experience compressive stress. The stress-strain analysis of the middle bolt below refers to the bolt subjected to the most significant tensile force, the B3 bolt.

4.3.1. Stress analysis

The equivalent stress nephogram of the B3 bolt between flange-A and flange-B for each tested specimen is shown in Fig. 19. The peak stress in specimens J-1 and J-5 was observed to be centrally located within the bolt, diminishing progressively towards the ends of the bolt. In contrast, in specimens J-2 and J-4, the peak stress deviates slightly from the center. This variation is attributed to the differing contact degrees between the bolts and bolt-hole walls during loading.

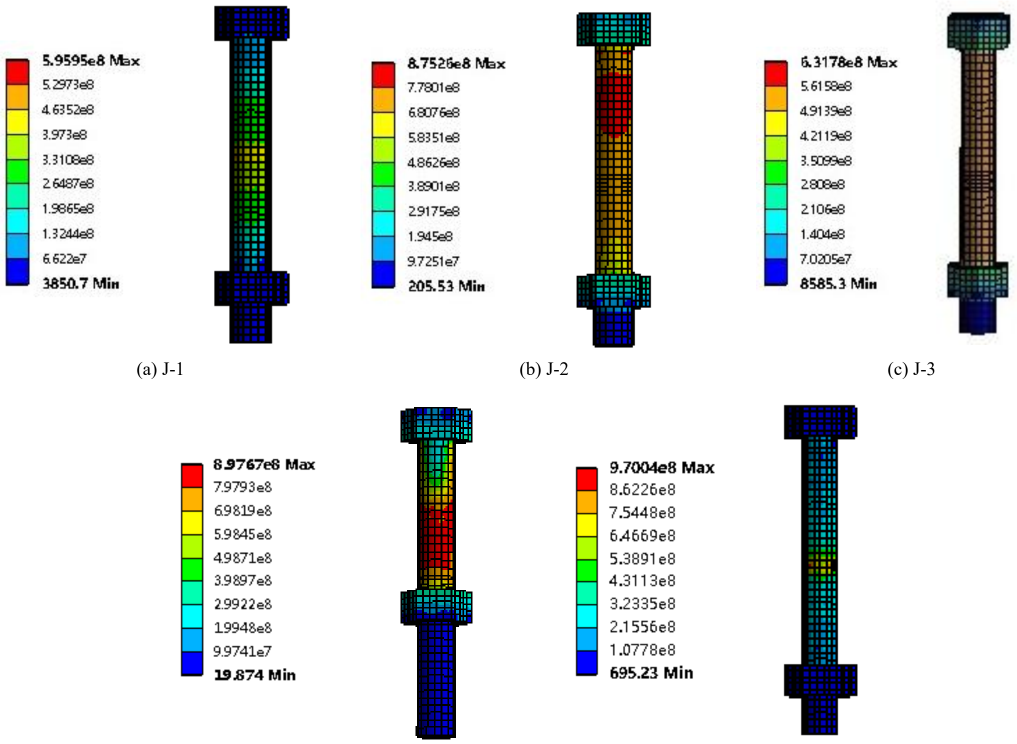

(a) J-1 (b) J-2 (c) J-3

(d) J-4 (e) J-5

Fig. 19 Equivalent stress nephogram of the B3 bolt between flange-A and flange-B

The maximum equivalent stress experienced by the B3 bolt between flange-A and flange-B in each specimen is shown in Fig. 20. Notably, among specimens J-1, J-2, and J-3, specimen J-2 exhibits the highest stress value 946.49 MPa. This indicates that the correlation between axial pressure and the maximum equivalent stress of the B3 bolt is not a direct linear relationship but exhibits an extremum at 600 kN. A reduction in flange thickness resulted in an elevated maximum equivalent stress at the bolt, reaching 950.96 MPa, 3.1% higher than specimen J-1. When the insertion depth is halved, the maximum equivalent stress of the B3 bolt escalated to 970.04 MPa, the highest among all specimens examined and 5.2% higher than specimen J-1. It is evident that diminishing the thickness of the flange, along with halving the insertion depth, induces considerable stress in the B3 bolt.

The equivalent stress nephogram for the compression side of the lower steel tube of each specimen is shown in Fig. 21. Examination of the figure reveals that the maximum equivalent stress for specimens J-1 and J-3 is located near flange-C at the bottom of the circular tube. In contrast, for specimens J-2, J-4, and J-5, the location of the maximum equivalent stress is less distinct, manifesting across a broader area.

The maximum equivalent stress identified in the compression side of the lower steel tube of each specimen is shown in Fig. 22. The data analysis reveals that specimens J-1, J-2, and J-3 exhibit similarly elevated stress levels. Specifically, specimen J-2 registers the minimum stress value at 474.58 MPa, while specimen J-3 records the maximum at 609.32 MPa. It is observed that reducing the flange thickness of the specimen results in the lowest equivalent stress on the compression side of the lower steel tube, measured at 356.05 MPa, which is 29.6% lower than that of specimen J-1. Furthermore, halving the insertion depth leads to a decrease in equivalent stress within this region to 367.31MPa, which is 27.4% lower than that of specimen J-1, although the extent of reduction is less pronounced than that observed in specimen J-4.

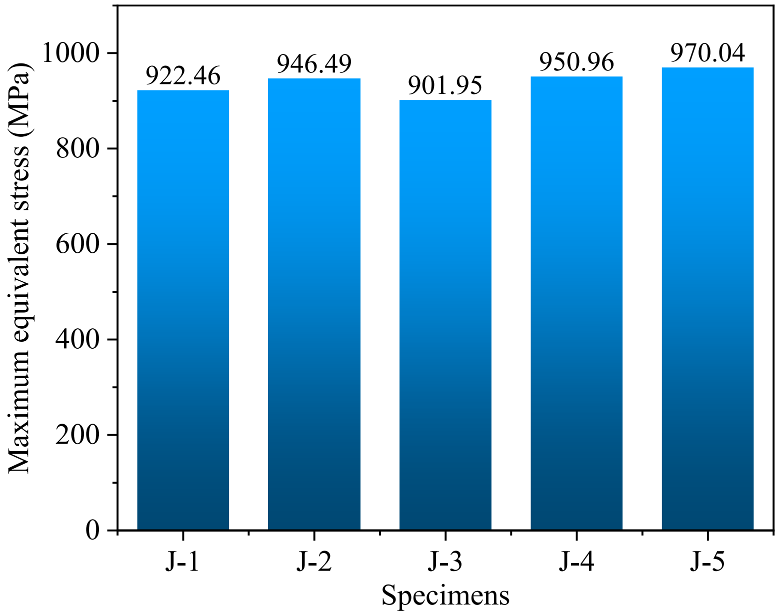

Fig. 20 Maximum equivalent stress at B3 bolt between flange-A and flange-B of each specimen

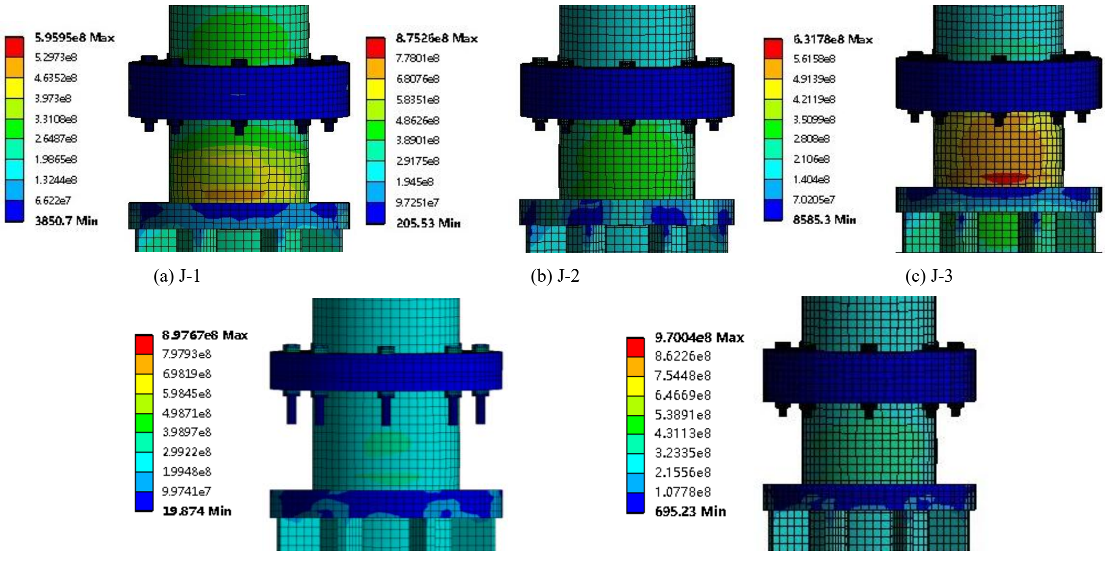

(a) J-1 (b) J-2 (c) J-3

(d) J-4 (e) J-5

Fig. 21 Equivalent stress nephogram of the compression side of the lower steel tube

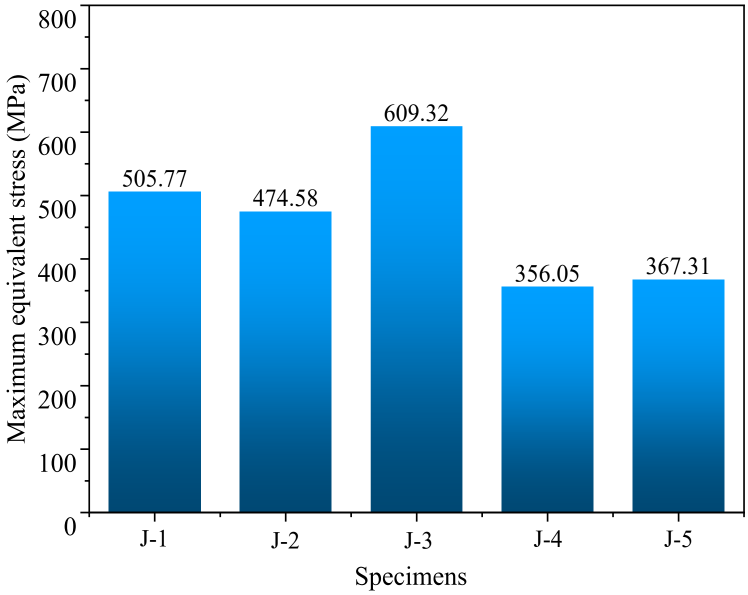

Fig. 22 Maximum equivalent stress at the compression side of the lower steel tube of each specimen

A critical observation concerns the contrasting pattern in the maximum equivalent stress observed at the B3 bolt compared to that at the compression side of the lower steel tube. Notably, at the B3 bolt, the stress value under an axial force of 600 kN surpasses those observed at 400 kN and 800 kN. Conversely, the stress values at the compression side of the lower steel tube exhibit an opposite trend. Furthermore, while reducing the flange thickness and halving the insertion depth elevate the stress at the bolt, these modifications lead to a reduction in stress at the compression side of the lower steel tube. This inverse correlation underscores the intricate interplay between structural alterations and their impact on the internal stress distribution within the specimens.

4.3.2. Strain analysis

The equivalent plastic strain of each specimen on the compression side and the B3 bolt at the turning point is shown in Fig. 23. It can be seen that plasticity only occurs in a small part of specimens J-1, J-2, and J-3, and most of the other parts do not enter the plasticity stage. Specimens J-1 and J-3 enter the plastic state from the middle of the B3 bolt, while specimen J-2 enters the plastic stage from the bottom of the steel tube near flange-C. The plastic development of specimens J-1, J-2, and J-3 at the turning point obtained by numerical simulation is in good agreement with the load-displacement curve obtained by the test, as it is evident from the curve that the specimens are transitioning from the elastic stage to the plastic stage at this time. The plastic development of specimens J-4 and J-5 is more complete, indicating that the plastic deformation of joints in the numerical simulation occurs earlier than in the test.

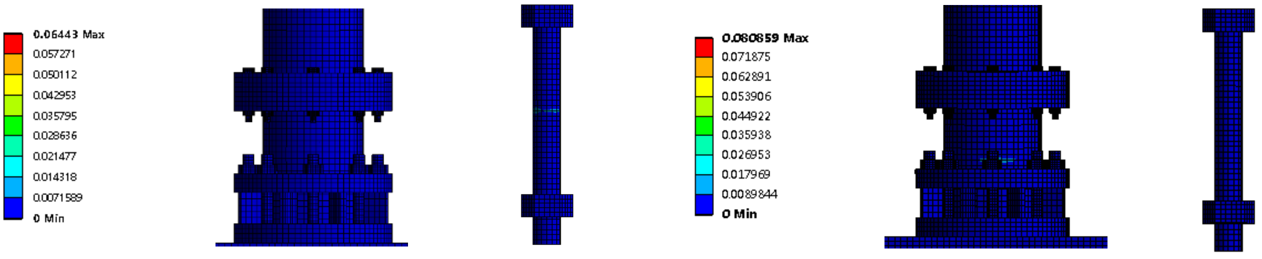

(a) J-1 (b) J-2

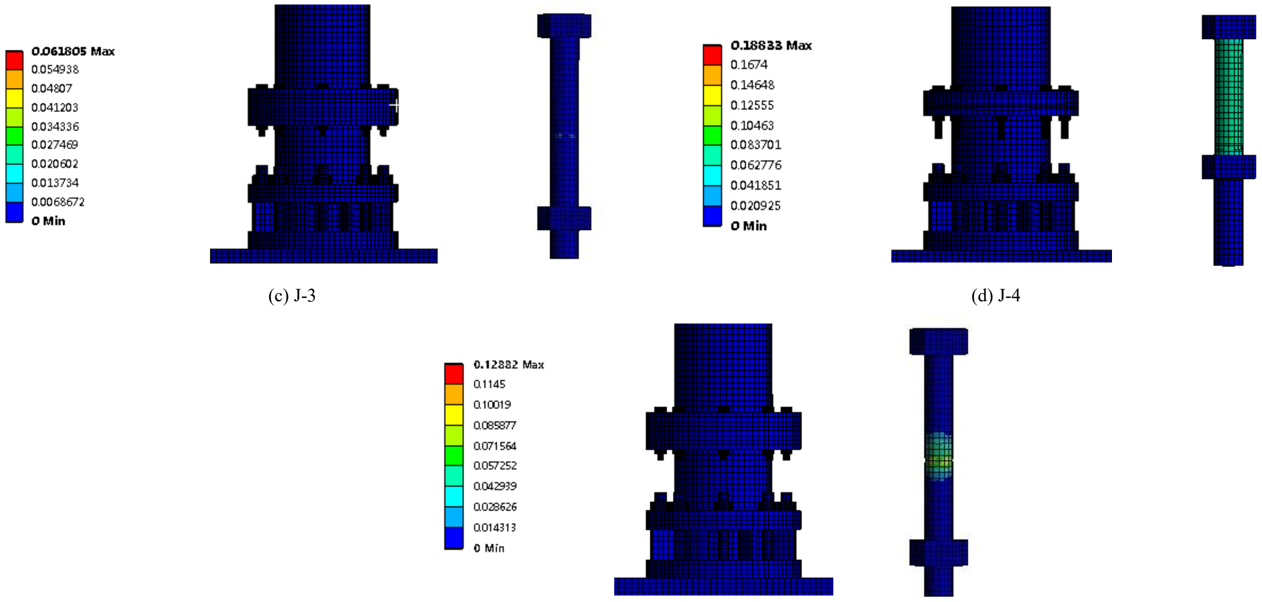

(c) J-3

(d) J-4

(e) J-5

Fig. 23 Equivalent plastic strain nephogram of the joints on the compression side and the B3 bolt at the turning point

The equivalent plastic strain nephogram of the B3 bolt between flange-A and flange-B for each specimen was shown in Fig. 24. As observed in the figure, the plastic strain in specimens J-1 and J-5 is confined solely to the midsection of the bolt. This localization of plasticity correlates with the observed stress distribution within the bolt. Specimen J-3 exhibits minimal plastic deformation, with only a small portion of the bolt undergoing plasticity. Notably, specimens J-2 and J-4 demonstrate plastic deformation throughout the entire bolt rod, indicating a more widespread strain distribution under the applied conditions. This variation in plastic strain among the specimens aligned with the differences in stress distribution, highlighting the impact of structural and loading variations on the deformation characteristics of the bolt.

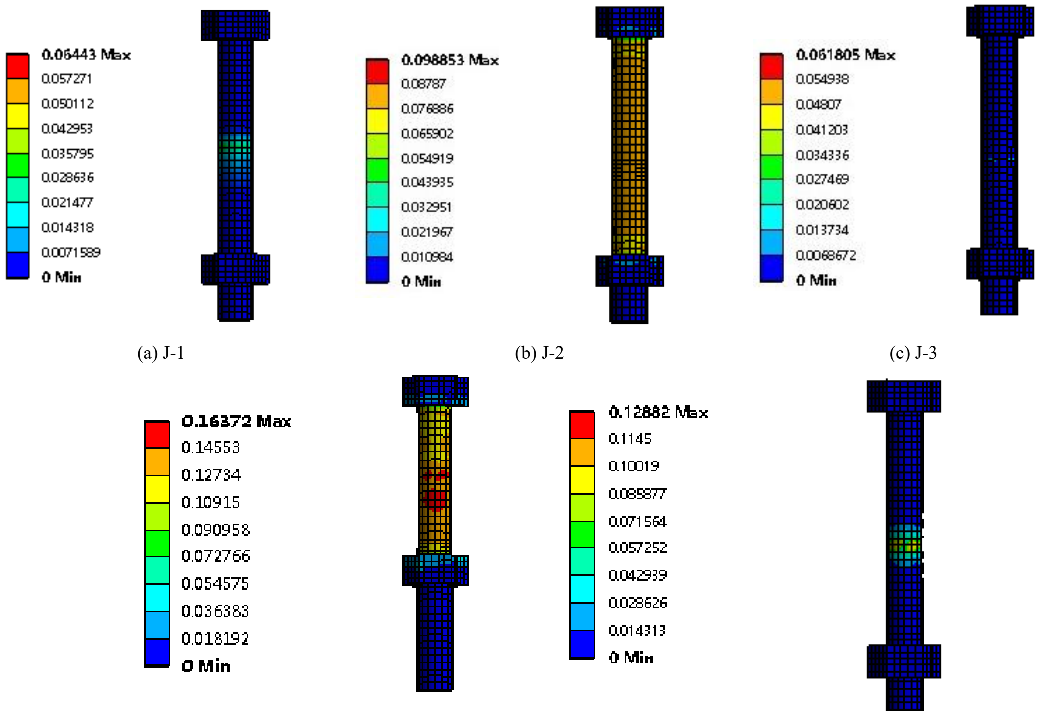

(a) J-1

(b) J-2

(c) J-3

(d) J-4

(e) J-5

Fig. 24 Equivalent plastic strain nephogram of the B3 bolt between flange-A and flange-B

The maximum equivalent plastic strain value of the B3 bolt between flange-A and flange-B of each specimen is shown in Fig. 25. As can be seen from the figure, the maximum equivalent plastic strain value of the B3 bolt for specimens J-1, J-2, and J-3 with different axial pressure parameters is at a low level, not exceeding 0.1. When the flange thickness of the specimen decreases, the maximum equivalent plastic strain at the bolt of the specimen reaches 0.1483, which is 5.2 times that of the specimen J-1. After the insertion depth of the specimen is halved, the maximum equivalent plastic strain at the bolt of the specimen is 0.1259, which is 4.4 times that of the specimen J-1. In both cases, the strain of the bolt reaches a considerable value, indicating relatively sufficient plastic deformation.

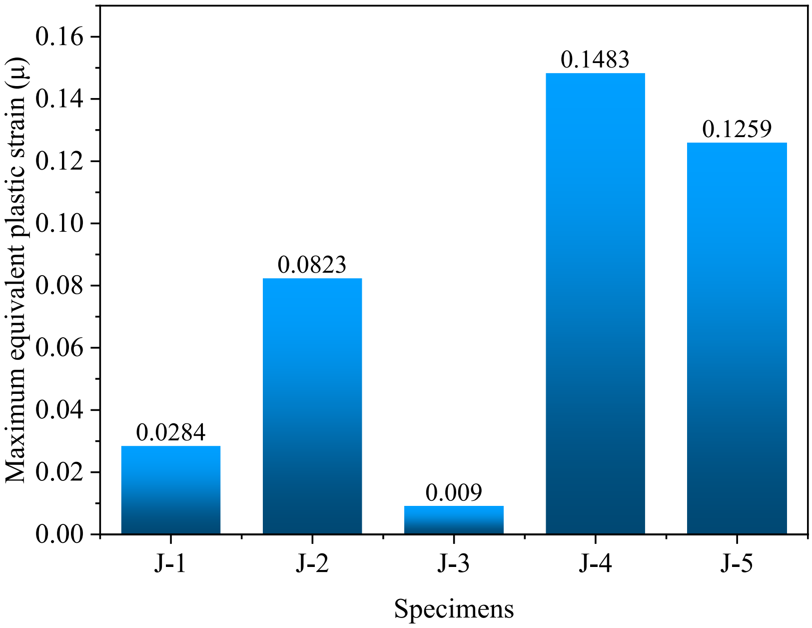

Fig. 25 Maximum equivalent plastic strain at the B3 bolt between flange-A and flange-B of each specimen

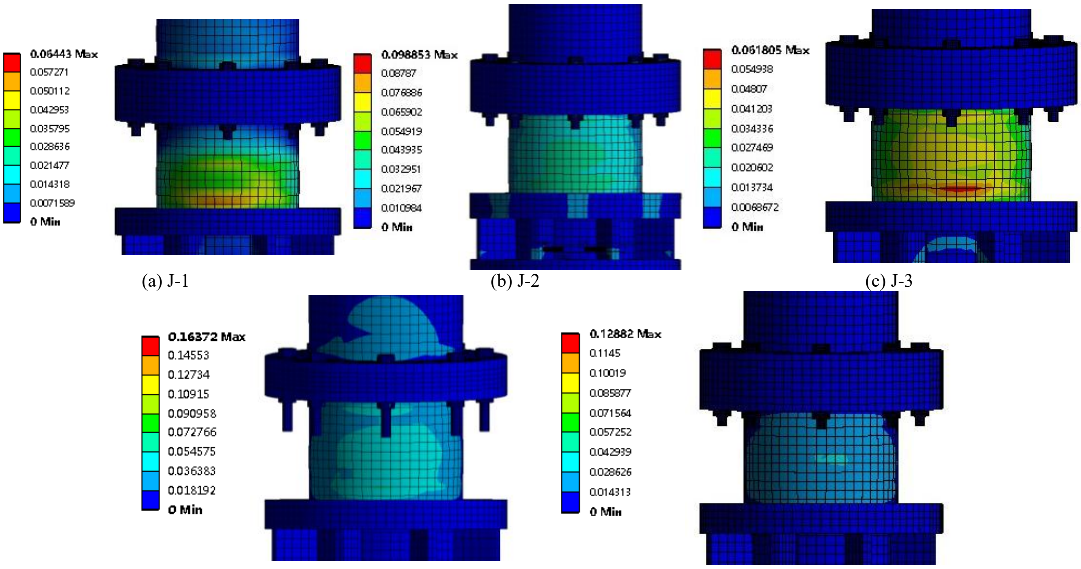

(a) J-1 (b) J-2 (c) J-3

(d) J-4 (e) J-5

Fig. 26 Equivalent plastic strain nephogram of the compression side of the lower steel tube

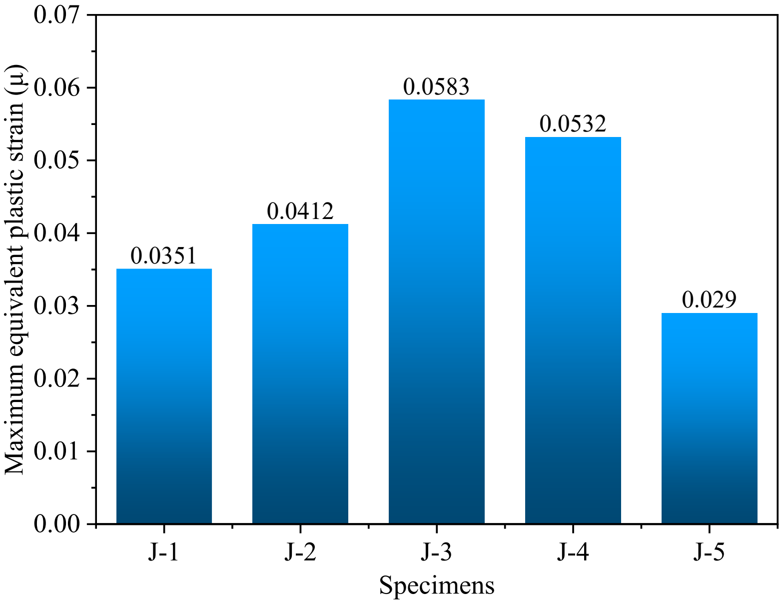

Fig. 27 Maximum equivalent plastic strain at the compression side of the lower steel tube of each specimen

The equivalent plastic strain distribution on the compression side of the lower steel tube is shown in Fig. 26. It is evident from the figure that all specimens have entered a plastic state. Specimens J-1 and J-4 exhibit plastic deformation on both the upper and lower sides of flange-A and flange-B, and the maximum plastic strain is observed at the bottom of the steel tube near flange-C. The distribution of plastic strain in specimen J-3 is similar to specimen J-1, with the maximum value of plastic strain also appearing at the bottom of the steel tube near flange-C. The distribution of plastic strain in specimen J-3 is similar to specimen J-11, with the maximum value of plastic strain also appearing at the bottom of the steel tube near flange-C. However, no plastic strain is evident on the upper side of flange-A. For specimen J-4, when the plastic strain appears on the upper side of flange-A, there is no distinct extreme value, and the plastic strain distribution is relatively uniform. The strain distribution of specimens J-3 and J-5 is similar, with plastic strain only appearing on the lower side of flange-B.

The maximum equivalent plastic strain on the compression side of the lower steel tube of each specimen is illustrated in Fig. 27. It is evident from the figure that as the axial pressure on the specimen increases, the plastic strain of the compression side of the lower steel tube increases. This is due to the rise of the axial pressure acting on the top of the joint. The magnitude of the axial pressure directly affects the stress condition at the bottom of the joint. The maximum equivalent plastic strain of specimen J-4 reaches 0.0532, which is 51.6% larger than specimen J-1. Reducing the thickness of the flange increases the plastic strain on the compression side of the lower steel tube of the joint. The maximum equivalent plastic strain of specimen J-5 is 0.0290, which is a reduction of 17.4% compared to specimen J-1. Reducing the inserting depth decreases the plastic deformation on the compression side of the lower steel tube of the joint.

5. Parametric analysis

To further investigate the influence of various parameters on the mechanical strength and rotation capacity of the proposed joints, multiple sets of specimens were prepared in each group for numerical analysis, considering the two parameters of tube wall thickness and the outside diameter of flanges A and B.

5.1. Effect of tube wall thickness

Seven joint specimens with varying tube wall thicknesses were analyzed using the finite element method. The tube wall thicknesses are 6 mm, 8 mm, 10 mm, 11 mm,12 mm,13 mm, and 14 mm, respectively. All other parameters of the specimens are identical to those of specimen J-1. The specific sizes of all specimens are shown in Table 7.

The moment-rotation curve derived from the numerical simulation results of the specimens is shown in Fig. 28. The Farthest Point Method was adopted [44] to determine the mechanical properties of the joints, as shown in Fig. 29, and the initial stiffness, yield moment and corresponding yield rotation, and ultimate moment and corresponding ultimate rotation of each joint were given, as shown in Table 8.

The data presented in Table 8 clearly show that the mechanical parameters of the joints exhibit a specific trend as the joint wall thickness increases. Initially, as the wall thickness increases from 6 mm to 10 mm, all the mechanical parameters, including the initial stiffness, yield moment, yield rotation, ultimate moment, and ultimate rotation, continuously increase, reaching a local maximum value at 10 mm. This indicates that a thicker wall enhances the overall mechanical performance of the joint. However, a different pattern emerged as the wall thickness increased from 10 mm to 12 mm. In this range, all the mechanical parameters of the joint start to decrease continuously, reaching a local minimum value at 12 mm. This indicates that there is an optimal range for the wall thickness, beyond which increasing the thickness is not advantageous for enhancing the mechanical properties of the joint. Interestingly, when the wall thickness increased from 12mm to 14 mm, the mechanical parameters of the joint started to increase again, continuing to rise and reaching the maximum value at 14 mm. This suggests that there may be additional benefits to increasing the wall thickness beyond the optimal range.

Table 7
Detailed information of the specimens

Specimen No.	t (mm)	h (mm)	F (kN)	s (mm)
J-t-6	6	30	400	200
J-t-8	8	30	400	200
J-t-10	10	30	400	200
J-t-11	11	30	400	200
J-t-12	12	30	400	200
J-t-13	13	30	400	200
J-t-14	14	30	400	200

Note: The naming rule of the seven specimens is J + t + tube wall thickness, where J stands for joint and t for wall thickness.

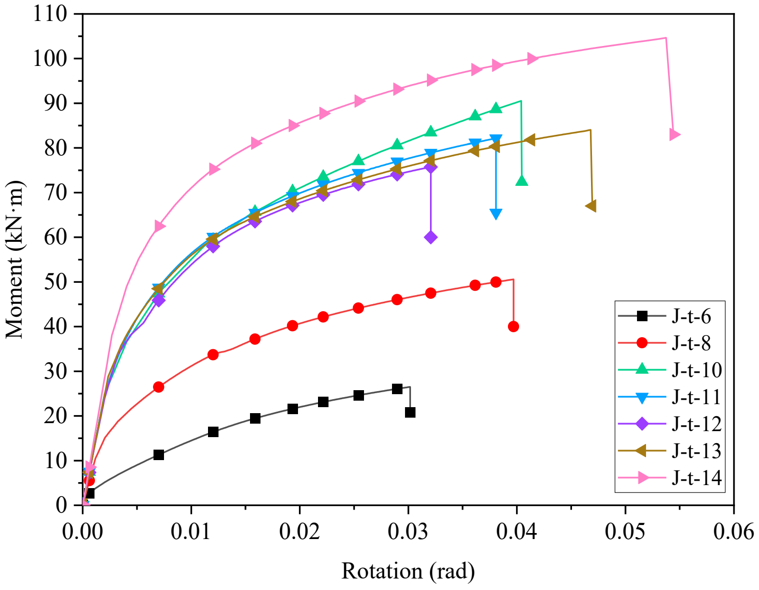

Fig. 28 Moment-rotation curve of the joints

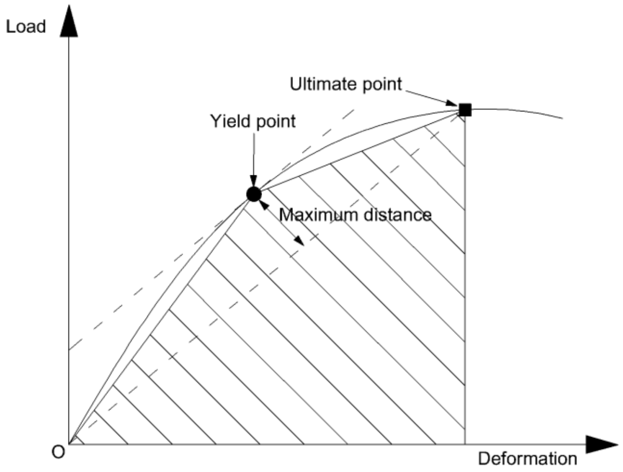

Fig. 29 Farthest Point Method for determination of yield points of members

Table 8
Mechanical properties of the specimens

Specimen No.	K_0(kN·m/rad)	M_y(kN·m)	θ_y(rad)	M_u(kN·m)	θ_u(rad)
J-t-6	4428	2.69	0.00061	26.50	0.03017
J-t-8	8788	32.56	0.01103	50.58	0.03970
J-t-10	12395	58.03	0.01119	90.54	0.04040
J-t-11	11957	55.63	0.00965	82.15	0.03807
J-t-12	11815	52.85	0.00957	75.75	0.03207
J-t-13	12150	58.21	0.01119	84.05	0.04680
J-t-14	14289	74.34	0.01155	104.66	0.05374

Considering both the joint performance and economical cost, selecting a wall thickness of 10 mm as the most appropriate value is advisable. At this thickness, the mechanical properties of the joint reach their local maximum, indicating optimal performance and choosing a thickness of 10 mm balances the mechanical capabilities and the economic cost of manufacturing. It is important to note that the specific performance requirements, design constraints, and application context should be considered when determining the suitable wall thickness for a joint in a practical situation.

5.2. Effect of flange outside diameter

Five joint specimens with different outer diameters of flange-A and flange-B were analyzed using the finite element method. The outer diameters of the flanges are 252 mm, 264 mm, 276 mm, 288 mm, and 300 mm, respectively. Other parameters of the specimens are identical to those of J-1. The specific dimensions of all specimens are shown in Table 9.

Table 9
Detailed information of the specimens

Specimen No.	d（mm）	t (mm)	h (mm)	F (kN)	s (mm)
J-d-252	252	10	30	600	200
J-d-264	264	10	30	600	200
J-d-276	276	10	30	600	200
J-d-288	288	10	30	600	200
J-d-300	300	10	30	600	200

Note: The naming rule of the five specimens is J + d + flange diameter, where J stands for joint and d for diameter.

Based on the numerical analysis results, the moment-rotation curves of five joint specimens were plotted, as shown in Fig. 30. The farthest point method was applied to determine the yield moment and corresponding yield rotation, ultimate moment and corresponding ultimate rotation, and initial stiffness of the joint specimens, as shown in Table 10. From the information provided in Fig. 30, it is evident that the joint labeled J-d-252 exhibits the highest initial stiffness and ultimate bending moment. As the outer diameters of Flange-A and Flange-B increase, the bearing capacity of the joints decreases compared to the J-d-252 joint. Specifically, when the outer diameter of the joint flange increases from 264 mm to 300 mm, the yield strength and ultimate strength remain nearly unchanged at approximately 54 kN·m and 80 kN·m, respectively. Additionally, the yield and ultimate rotation do not significantly differ, except for a slight reduction in the yield and ultimate rotation of J-d-300.

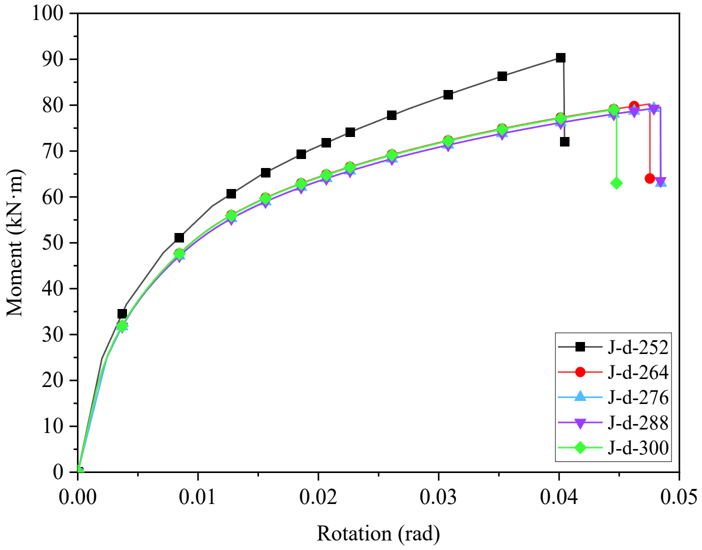

Fig. 30 Moment-rotation curves of the joints

Considering both the mechanical properties of the joint and economic factors, selecting the outer diameter of the flange as 252mm is recommended. The J-d-252 joint exhibits the most significant initial stiffness and ultimate bending moment among the tested joints. While increasing the outer diameter of the flange may not significantly impact the yield strength, ultimate strength, yield angle, or ultimate rotation, it results in a decrease in bearing capacity compared to the joint J-d-252.

However, it is essential to note that the specific application, design requirements, and constraints should be carefully considered when determining the appropriate outer diameter of the flange for a joint. Other factors, such as cost-effectiveness and additional performance considerations, should also be considered when making the final decision.

Table 10
Mechanical properties of the specimens

Specimen No.	K_0(kN·m/rad)	M_y(kN·m)	θ_y(rad)	M_u(kN·m)	θ_u(rad)
J-d-252	12395	58.03	0.01119	90.54	0.04040
J-d-264	11349	54.31	0.01167	80.23	0.04755
J-d-276	10397	53.61	0.01167	79.48	0.04843
J-d-288	11483	53.33	0.01152	79.48	0.04843
J-d-300	11455	53.59	0.01129	79.09	0.04478

6. Conclusions

In this study, the experimental research and finite element analysis of the proposed joint used for advanced automation devices were conducted under combined vertical and lateral loads. Based on the experimental observation and finite element analysis, the following conclusions can be drawn:

1. Axial force has a limited impact on the ultimate moment of the joint but significantly reduces the ultimate rotation. Thinner flanges A and B cause a 15.7% drop in the ultimate moment and a 34.1% rise in the ultimate rotation. Halving the insertion depth leads to a 44.9% rise in the ultimate moment and a 31.5% rise in the ultimate rotation. Additionally, the failure of all specimens is due to the bolt connection, specifically the failure of the threads. However, no significant damage is found in the joint tube wall, indicating that the failure primarily occurs in the bolt connection.
2. The moment-rotation curve and mechanical parameters derived from the experimental and numerical simulation studies exhibit a high degree of consistency. At the turning point, the progression of plastic deformation in simulated specimens with different axial forces aligns well with the experiment results. However, in the numerically simulated specimens with thinner flanges and shorter insertion depth, the onset of plastic deformation of the joint occurs earlier than in the experimental specimens. This discrepancy may be due to the simplification of the bolt model and the selection of the standard friction coefficient.
3. The maximum equivalent stress at the B3 bolt initially increases by 2.6% and then decreases by 2.2% with increasing axial force. The thinner flange increases the stress at the B3 bolt by 3.1 % due to the diminished contact area between the bolt and flange resulting from decreased flange thickness, which enhances the stress concentration. A shorter inserting depth increases the stress at the B3 bolt by 5.2%, a consequence of the diminished support provided by the inserting portion to the upper steel tube, necessitating the bolts to withstand increased loads. Conversely, the maximum equivalent stress evolution trend on the compression side of the lower steel tube is opposed to that of the B3 bolt.
4. The maximum equivalent strain at the B3 bolt initially increases and then decreases with the increasing axial force, while on the compression side of the lower steel tube, it consistently increases. The equivalent strain at the B3 bolt in three of the five specimens exceeds that on the compression side of the lower steel tube, suggesting a higher failure risk at the bolts, which aligns with observed bolt loosening in the experiments. When the axial pressure is 800 kN, the compression side of the lower steel tube may fail earlier due to the high axial pressure. When the axial pressure is 400kN, this discrepancy may be attributed to the simplification of bolt modeling and the selection of the standard friction coefficient values.
5. The mechanical properties of the joint fluctuate with increasing tube wall thickness, peaking at 10 mm, which optimally balances the mechanical properties and economic cost. The bearing capacity of the joint decreases with increasing outer diameters of flange-A and flange-B. Considering both the mechanical performance and the financial cost of the joint, selecting a flange with an outer diameter of 252 mm is recommended.

The findings in this study indicate the influence of various factors and parameters, such as bolt connection, axial force, flange thickness, wall thickness of the circular tube, and flange diameter, on the bearing and rotation capacities of the joint. Understanding these relationships should be beneficial to designing and optimizing the joint for the desired performance. Although this paper has made efforts to study the joint of the automated construction device, there are still some shortcomings that need to be addressed. Future research could focus on exploring the mechanical response of the joint under dynamic loads or investigating the mechanical properties of the joint when utilizing new materials. Such studies will provide a deeper understanding of joint performance and durability, potentially leading to further improvements in the design and functionality of automated construction systems.

Acknowledgments

The authors gratefully acknowledge the financial support provided by the National Key R&D Program of China (2022YFE0109300), Shenzhen Natural Science Foundation (JCYJ20240813141827036), Shenzhen Housing and Construction Bureau - Science and Technology Program in Engineering Construction Field (2021-R&D), Guangdong Provincial Key Laboratory of Durability for Marine Civil Engineering (2020B1212060074), and Shenzhen Key Laboratory for Low-carbon Construction Material and Technology (ZDSYS20220606100406016).

References

[1] Elkhalifa A., "The magnitude of barriers facing the development of the construction and building materials industries in developing countries, with special reference to Sudan in Africa", Habitat International, 2016, Vol. 54, PP. 189-198.
[2] Jiang, Z.Y., Sun, X.P., Luo, Y.Q., Fu, X.L., Xu, A. and Bi, Y.Z., "Recycling, reusing and environmental safety of industrial by-product gypsum in construction and building materials", Con-struction and Building Materials, 2024, Vol. 432.
[3] Senthamizh, S.S., Anandh, K.S., "Navigating leadership styles through qualitative exploration for enhanced safety in the construction sector", Safety Science, 2024, Vol. 175.
[4] Zhang, M., Shi, R. and Yang, Z., "A critical review of vision-based occupational health and safety monitoring of construction site workers", Safety Science, 2020, Vol. 126.
[5] Zhao, X., Jin, Y., Selvaraj, N.M., Ilyas, M. and Cheah, C.C., "Platform-independent visual installation progress monitoring for construction automation", Automation in Construction, 2023, Vol. 154.
[6] Zhang, M., Xu, R., Wu, H., Pan, J. and Luo, X., "Human–robot collaboration for on-site construction", Automation in Construction, 2023, Vol. 150.
[7] Xiao, B., Chen, C. and Yin, X., "Recent advancements of robotics in construction"., Automation in Construction, 2022, Vol. 144.
[8] Oke, A.E., Aliu, J., Oluwasefunmi, F.P., Akanni, P.O. and Stephen, S.S., "Attaining digital transformation in construction: An appraisal of the awareness and usage of automation techniques", Journal of Building Engineering, 2023, Vol. 67.
[9] Bogue, R., "What are the prospects for robots in the construction industry?", Industrial Robot-An International Journal, 2018, Vol. 45, PP. 1-6.
[10] Rosa, M., Cury, J.E.R. and Baldissera, F.L., "Supervisory Control in Construction Robotics: in the Quest for Scalability and Permissiveness", IFAC-PapersOnLine, 2020, Vol. 53, PP. 117-122.
[11] Gharbia, M., Chang, R.A., Lu, Y., Zhong, R.Y. and Li, H., "Robotic technologies for on-site building construction: A systematic review", Journal of Building Engineering, 2020, Vol. 32.
[12] Yu, Y., "What is Aerial Building Mechaine?", Hoisting Conveying Mach, 2017, Vol. 2017, PP. 39.
[13] Wakisaka, T., Furuya, N., Inoue, Y. and Shiokawa, T., "Automated construction system for high-rise reinforced concrete buildings", Automation in Construction, 2000, Vol. 9, PP. 229-250.
[14] Pan, C.L., Chen, S.M., Wang, G.F., Zhang, D.D. and Wei, X.H, "Construction technology of building structure under construction condition of integrated platform of Shenyang Baoneng Global Financial Center", Construction Technology, 2017, Vol. 46, PP. 18-20.
[15] Li, T.Z., "A new path for prefabricated construction—Aerial Building Mechaine", Construction Architecture, 2016, Vol. 22, PP. 43-44.
[16] Kudoh, R., "Implementation of an Automated Building Construction System", In Proc of 13th International CIB World Building Congress, Amsterdam, 1995.
[17] Dong, S.B., "Research on cast-in-situ prefabricated construction technology of Aerial Building Machine", Urban Architecture Space, 2017, Vol. 24, PP. 55-59.
[18] Pan, C.L., Quan, W.B., Zhang, W.S., Wang, G.F. and Chen, M.S., "Integrated platform technology for construction equipment of super high-rise building", Construction Technology, 2017, Vol. 46, PP. 1-4.
[19] Yin, L., Niu, Y., Quan, G., Gao, H. and Ye, J., "Development of new types of bolted joints for cold-formed steel moment frame buildings", Journal of Building Engineering, 2022, Vol. 50.
[20] Wei, J.P., Tian, L.M., Guo, Y., Qiao, H.Y., Bao, Y., Jiao, Z.A. and et al., "Numerical study of the seismic performance of a double-hinge steel frame joint", Journal of Constructional Steel Research, 2021, Vol. 187.
[21] Wang, H., Zhang, B., Qian, H., Liu, J., An, B. and Fan, F., "Experimental and numerical studies of a new prefabricated steel frame joint without field-welding: Design and static performance", Thin-Walled Structures, 2021, Vol. 159.
[22] Gao, J.D., Du, X.X., Yuan, H.X. and Theofanous, M., "Hysteretic performance of stainless steel double extended end-plate beam-to-column joints subject to cyclic loading", Thin-Walled Structures, 2021, Vol. 164.
[23] Chen, Z., Niu, X., Liu, J., Khan, K. and Liu, Y., "Seismic study on an innovative fully-bolted beam-column joint in prefabricated modular steel buildings", Engineering Structures, 2021, Vol. 234.
[24] Ma, Y., Qi, A., Yan, G., Zheng, L., Xue, P. and Wang, F., "Experimental study on seismic performance of novel fabricated T-joint with replaceable steel hinges", Structures, 2022, Vol. 40, PP. 667-678.
[25] Yan, X.Z., Zhe, W.H., Yang, L.L., Bo, W.J., Xiao, T.C. and Meng, Y.C., "Experimental and

numerical investigation of prefabricated prestressed vertical steel strand core tube flange column connection joint", Journal of Constructional Steel Research, 2022, Vol. 190, PP. 107-124.

[26] Fan, J., Yang, L., Wang, Y. and Ban, H., "Research on seismic behaviour of square steel tubular columns with deconstructable splice joints", Journal of Constructional Steel Research, 2022, Vol. 191.

[27] Havula, J., Garifullin, M., Heinisuo, M., Mela, K. and Pajunen, S., "Moment-rotation behavior of welded tubular high strength steel T joint", Engineering Structures, 2018, Vol. 172, PP. 523-537.

[28] GB/T8162-2018, "Seamless steel tubes for structural purposes", China. Beijing, Architecture & Building Press, 2018.

[29] GB/T1591-2018, "High strength low alloy structural steels", China. Beijing, Architecture & Building Press, 2018.

[30] Mou, B., Yan, X., Yu, Y. and Wang, Z., "Composite CFST column to H-shaped steel beam joint: Experimental and numerical investigation", Engineering Structures, 2024, Vol. 299.

[31] Li, Q., Xu, C., Luo, Z., Huang, F., An, Y., Zhang, D. and et al., "Experiment and design methodology of an IODR flange connection under bending load", Journal of Constructional Steel Re-search, 2023, Vol. 201, PP. 107-144.

[32] Fidalgo, A. and Packer, J.A., "Evaluation of bolted CHS flange-plate connections under axial tension", Journal of Constructional Steel Research, 2022, Vol. 196.

[33] Aydemir, C., Eser, A.M. and Arslan, G., "Seismic performance of RC columns under combined cyclic flexural and constant axial loadings", Structures, 2023, Vol. 54, PP. 196-208.

[34] Higgoda, T.M., Elchalakani, M., Kimiaei, M. and Guo, X., "Experimental and numerical investigation of bolted steel endplate with bonded sleeve end connections for pultruded GFRP circu-lar tubular hollow beams", Thin-Walled Structures, 2023, Vol. 192, PP. 111-133.

[35] Longo, A., Montuori, R. and Piluso,V., "Seismic reliability of chevron braced frames with innovative concept of bracing members", Advanced Steel Construction, 2009, Vol. 5, PP. 367-389.

[36] Jiang, Z.Q., Yan, T., Zhang, A.L., Yang, X.F., Yu, C. and Li, R., "Experimental study of plate-buckling type earthquake-resilient prefabricated steel beam-column joints with replaceable double flange cover plates", Structures, 2023, Vol. 50, PP. 110-113.

[37] Kashan, K. and Yan, J.B., "Numerical studies on the seismic behaviour of a prefabricated multi-storey modular steel building with new-type bolted joints", Advanced Steel Construction, 2021, Vol. 17, PP. 1-9.

[38] Sorace, S. and Terenzi, G., "Fluid viscous damper-based seismic retrofit strategies of steel structures: General concepts and design applications", Advanced Steel Construction, 2009, Vol. 5, PP. 325-342.

[39] Wang, H., Zhang, B., Qian, H., Liu, J., An, B. and Fan, F., "Experimental and numerical studies of a new prefabricated steel frame joint without field-welding: Design and static performance", Thin-Walled Structures, 2021, Vol. 159.

[40] Qin, Y., Chen, Z., Wang, X. and Zhou, T., "Seismic behavior of through-diaphragm connections between CFRT columns and steel beams-experimental study", Advanced Steel Construction, 2014, Vol. 10, PP. 351-371.

[41] Zhang, C. and Su, M., "Bearing capacity of bolted longitudinal seams of corrugated steel structures under compression", Journal of Constructional Steel Research, 2024, Vol. 213.

[42] Chen, Z., Qin, Y. and Wang, X., "Development of connections to concrete-filled rectangular tubular columns", Advanced Steel Construction, 2015, Vol. 11, PP. 408-426.

[43] GB/T1231-2006, "Specifications of high strength bolts with large hexagon head, large hexagon nuts, plain washers for steel structures", China. Beijing, Architecture & Building Press, 2006.

[44] Peng, F., Han, L.Q. and Lie,P.Y., "Discussion ang definition on yield points of materials, members ang structures", Engineering Mechanics, 2017, Vol. 34, PP. 36-46.